Physics – Uspekhi **66** (2) 148 – 172 (2023)

REVIEWS OF TOPICAL PROBLEMS PACS numbers: **05.45. – a**, 92.10.Hm

Rogue waves in the sea: observations, physics, and mathematics

A V Slunyaev, D E Pelinovsky, E N Pelinovsky

DOI: https://doi.org/10.3367/UFNe.2021.08.039038

Contents

Abstract. Rogue waves are anomalously high waves that may suddenly form on the sea surface. At the dawn of the 21st century, they attracted the interest of researchers, from oceanographers to mathematicians. The review discusses the results of their research: physical mechanisms leading to the generation of anomalously high waves and respective mathematical models, observational data, results of direct numerical simulations and laboratory experiments, and new approaches to modeling and forecasting extreme sea waves.

Keywords: rogue waves, freak waves, sea wind waves, nonlinear waves

1. Introduction

Descriptions of anomalous sea waves in the scientific literature go back more than half a century [1, 2], but *rogue waves* (also known as *freak waves*) received serious attention at the turn of the 20th to the 21st century, following the appearance of accurate instrumental measurements showing individual waves or short wave packets that significantly exceeded the background sea waves in height [3]. Rogue waves are considered to be the cause of some incidents with ships or shelf platforms (in particular, with the tanker *Prestige* (2002), the cruise ships *Norwegian Dawn* (2005) and *Louis Majesty* (2010), and the cargo ship *Cemfjord* (2015)) (see Refs [4–8] and also [9–10], which report on unexpected wave splashes on the shore). The possibility of describing anomalously high waves within the framework of spectral models of wind waves already used in oceanography and marine engineering is being questioned. For this reason, intensive work has been carried out over the last two decades on field measurements of sea waves, the development of new physical, mathematical, and probabilistic models, physical modeling, the consideration of associated loads, and the development of forecasting methods for sea waves. Reviews of current research on rogue waves can be found, for example, in monographs [5, 11–14] and articles [7, 15–19]. The aim of this review is, first and foremost, to discuss the results obtained in recent years in the design of physical and mathematical models for rogue waves and in the modeling of anomalous sea waves. Along with progress in the study of marine rogue waves, similar studies have been started in other branches of physics, most importantly in nonlinear optics (see [17, 20–22]). The specifics of optical rogue waves will not be discussed in this review.

The vast majority of marine field measurements, both past and present, are represented by time series of instantaneous water surface displacements at measurement points. Long records are divided into intervals of 10–30 min each, which are assumed to be statistically homogeneous. For each such

A V Slunyaev [(1,2,a)], **D E Pelinovsky** [(1,3,b)], **E N Pelinovsky** [(1,2,c)]
[(1)] Institute of Applied Physics, Russian Academy of Sciences, ul. Ul'yanova 46, 603950 Nizhny Novgorod, Russian Federation
[(2)] National Research University Higher School of Economics, ul. Bol'shaya Pecherskaya 25/12, 603155 Nizhny Novgorod, Russian Federation
[(3)] Department of Mathematics, McMaster University, 1280 Main Street West, Hamilton, Ontario L8S 4K1, Canada
E-mail: [(a)] slunyaev@ipfran.ru, [(b)] dmpeli@math.mcmaster.ca, [(c)] pelinovsky@ipfran.ru

Received 24 July 2021, revised 6 August 2021
Uspekhi Fizicheskikh Nauk **193** (2) 155 – 181 (2023)
Translated by S D Danilov

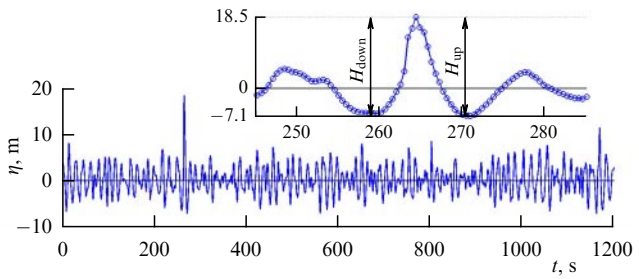

Figure 1. New Year Wave record: surface displacement at a measurement point as a function of time. Inset shows the heights of an anomalous wave determined according to the *down-crossing* and *up-crossing* methods, H_{down} and H_{up}.

interval, the record is further subdivided into individual waves based on crossings of the unperturbed surface. The main characteristics of individual waves are their periods and heights. The latter are calculated as the vertical distance between the upper point (crest) and the lower point (trough) of an individual wave (see inset in Fig. 1). There are different implementations of this procedure [23], resulting in slightly different estimates of periods and wave amplitudes.

Figure 1 shows the best known example of an anomalous high wave — the so-called New Year Wave recorded with a laser altimeter at the Draupner platform in the North Sea on January 1, 1995 [24]. It shows a 20-min surface displacement record and also the interval with the anomalous wave. The measurement frequency of 2.1 Hz ensures a sufficiently detailed description of the wave profile (circles in the inset). The height of the New Year Wave, estimated to be $H = 25.6$ m, is well above the level of the background sea waves.

A traditional first approximation for describing sea waves is to represent them as a superposition of independent random sinusoidal waves. In this case, by virtue of the central limit theorem, the sea surface displacement obeys Gaussian statistics and, assuming that the wave spectrum is sufficiently narrow, the probability of measuring a wave with a height not less than H is described by the Rayleigh distribution [25]

$$P(H) = \exp\left(-\frac{H^2}{8\sigma^2}\right), \tag{1}$$

where σ^2 is the variance of the surface displacement. In oceanography, the characteristic (so-called *significant*) wave height H_s is routinely defined as the average over one third of the highest waves in the record, $H_{1/3}$. In the case of a narrowband spectrum, this quantity is related to the root mean square displacement as $H_{1/3} \approx 4.004\sigma$. If the spectrum is not narrow enough, a modification of formula (1) is used,

$$P(H) \approx \exp\left(-2\,\frac{H^2}{H_s^2}\right), \tag{2}$$

in which case the use of $H_s = H_{1/3}$ reduces the contribution of small-scale waves to the mean height estimate and leads to better agreement with direct modeling results.

A parameter AI (*amplification index* or *abnormality index*) is introduced as a characteristic of the 'abnormality' of a high wave, describing the excess with respect to the background sea waves,

$$\mathrm{AI} = \frac{H}{H_s}, \tag{3}$$

where the significant height H_s is defined as $H_s = H_{1/3}$ or $H_s = 4\sigma$. The definition most commonly used in the literature to single out the class of 'rogue waves' sets the minimum required excess height at $\mathrm{AI} > 2$. Alternative definitions of marine rogue waves could use different thresholds of AI, impose additional constraints (on the absolute magnitude and asymmetry of the wave), be formulated for the crest height, and so on. In this review, the definition of rogue waves will be based on the AI criterion for wave height (3) or a similar criterion for the wave amplitude amplification factor (39).

The probability distribution for the wave height (2) describes the real situation quite well if the events are not too rare and respectively the waves are not too high [25]. Based on the probability distribution (2), it is easy to estimate the recurrence rate of anomalous wave events for the parameter AI (3) introduced above. For the New Year Wave, $H_{1/3} \approx 11.4$ m and $H/H_{1/3} \approx 2.24$; hence, it follows that it corresponds to an event with probability 4×10^{-5}, i.e., one wave in 20 thousand. If we assume that the period of sea waves is 10 s, we find that a wave with the index $\mathrm{AI} = 2.24$ has a return period of less than 3 days. Similarly, waves with $\mathrm{AI} = 2$ should be recorded 2–3 times per day. Since the absolute value of the wave height is important from a practical point of view, which is not taken into account by the AI parameter, dangerous rogue waves are much rarer in real life.

The problem of rogue waves on the sea surface can be statistically formulated as the description of probabilistic wave properties (wave heights, amplitudes of crests and troughs, etc.) in the conditional range of rogue waves $\mathrm{AI} > 2$; the Rayleigh distribution is commonly used as a reference. In practical applications, within the framework of quadratic weakly nonlinear theory, one takes into account the deviation of the wave shape from a sinusoidal one, which above all modifies the probability distributions for the amplitudes of the crests and troughs, but not for the heights. Rogue waves are not described by second-order statistical models. Section 2 discusses the fact that, despite the huge amount of instrumental measurements of sea waves (several hundred million individual waves), there is no reliable statistical description in the domain of rogue waves. It also presents the available eyewitness observations of anomalously high waves.

The deviations of wave statistics from Gaussian can be conveniently estimated through the values of statistical moments. The variance is defined through the root mean square deviation of the surface η: $\sigma^2 = \langle \eta^2 \rangle$ with zero mean, $\langle \eta \rangle = 0$; the third and fourth statistical moments λ_3, λ_4 are defined as

$$\lambda_3 = \frac{\langle \eta^3 \rangle}{\sigma^3}, \qquad \lambda_4 = \frac{\langle \eta^4 \rangle}{\sigma^4}. \tag{4}$$

It is well known that for a Gaussian random value $\lambda_3 = 0$, $\lambda_4 = 3$. The deviations in the measured values from these values imply that the waves are vertically asymmetric and have an altered balance between the proportions of small and large displacements (the quantity $\lambda_4 - 3$ is called the excess kurtosis).

In a dynamical sense, the problem of rogue waves can be understood as a search for possible mechanisms of rapid and significant wave amplification (see the discussion in Section 3). First of all, the literature was concerned with linear wave

focusing mechanisms and the effects of wave amplification on currents. Since the processes of random wave superposition are already accounted for in Gaussian statistics, other effects leading to wave amplification are important. This review focuses on wave growth mechanisms resulting from 'fast' nonlinear wave interactions, which are new for oceanography initiated by, among other things, variable conditions (rough bottom, ambient currrents, or variable wind). These effects are not taken into account in the kinetic equations used by forecasting centers to model sea waves. The most impressive series of studies is related to the 'rediscovery' of the effect of modulation instability of sea waves, which seems to be the most likely candidate for the role of a universal mechanism that increases the probability of anomalously high waves under certain conditions.

Most of the research on rogue waves is carried out for the deep sea. In this limit, the water depth drops out of the parameter set and three-wave interactions only lead to a modification of the wave shape. In the case of shallow basins, the displacement obeys the Gaussian distribution only for very small amplitude waves. The modulation instability present in deep water disappears in shallow water. However, the effects of nonlinear dynamics in shallow water can also lead to a significant increase in the probability of high waves. Waves propagating under variable depth conditions may be affected by different nonlinear amplification mechanisms. These effects are also discussed in Section 3.

The use of integrable nonlinear models as a first approximation to describe rogue wave effects allows the application of the inverse scattering transform and related exact methods to obtain model analytical solutions and effective descriptions of nonlinear waves and their ensembles [26–28]. References [29, 30] proposed using breather solutions to the nonlinear Schrödinger equation (NSE) [31–34] as models for rogue waves, realizing a nonlinear mechanism for the occurrence of unexpectedly high waves that "appear from nowhere and disappear without a trace" [35]. Later, this class of solutions was extended to include new solutions of the NSE as well as other integrable equations describing a nonlinear stage in the development of the instability of sinusoidal and nonsinusoidal waves. The class of such solutions to nonlinear equations is called rogue wave solutions: they have already lost their physical 'roots' and are studied as independent mathematical objects. The correspondence between the modulation instability and rogue wave-type solutions has been demonstrated, and a universal description of the modulation instability has been obtained. These results are discussed in Section 4.

Due to the difficulties mentioned above in finding a probabilistic description of rogue waves based on field data, special attention has been given to modeling in the framework of laboratory experiments and numerical simulation. Wave evolution computations in the framework of spectral energy balance equations, which are currently used for operational forecasting, are based on assumptions of weak nonlinearity, quasi-stationarity, and independence of random wave phases [36]. Kinetic models are unable to account for rogue waves, and direct (phase-resolving) numerical simulation of the full hydrodynamic equations is required. Furthermore, fast numerical codes are needed to simulate large statistical ensembles [37, 38]. The methods of integrating hydrodynamical equations used for stochastic (Monte Carlo) modeling of sea waves are presented in Section 5. Further, this section discusses the results of numerical simulations for ensembles of irregular waves: the observation of fast wave evolution, probability distributions, as well as characteristic patterns of rogue waves: the shape of extreme waves and the duration of events.

A discussion of the general picture of the obtained results, open problems, and prospective directions in rogue wave research is given in the Conclusions (Section 6). In addition to obtaining the calculated characteristics of extreme waves, it is practically important to be able to predict dangerous waves on various time horizons, performing deterministic forecasting in short times (several minutes) and probabilistic forecasting at longer time intervals.

2. Data from observations and records of rogue waves

Reports about sudden waves damaging ships and constructions in the open sea and onshore and sweeping people off the coast appear in the media almost every week. Among recent cases: on January 16, 2011 the 114-meter-long cargo ship *Arvin* was split in two by a wave in the Black Sea off the Turkish coast and sank, with only six of its 13 crew members rescued [39]. On January 4 of the same year, a sudden wave washed two children off the coast of California; their father died trying to save them [40]. A large number of descriptions, photos, and videos of such events and waves can be found on the Internet. Over the last 20 years, attempts have been made to compile and analyze similar cases of rogue waves [8–10, 41–47]. The catalogues compiled contain detailed descriptions of the events that occurred, and also some of their characteristics reported by witnesses and available data (meteorological records, re-analysis of the state of the sea in the area, etc.). The height criterion (3) is usually used to define rogue waves, although the information on wave amplitude is not always known with certainty. Besides, the media generally cover events that create the largest damage, irrespective of the wave height.

The latest catalogue [8] contains descriptions of 210 events for the period 2011–2018, which corresponds on average to one event every three weeks. The geographical distribution of the observed rogue waves is shown in Fig. 2a. Its inhomogeneity is related to the connection to major shipping routes in the world's oceans, as well as differences in population density in coastal areas and the difficulty in finding information in non-English media. Figure 2b illustrates the distribution of recorded cases across observation locations: deep or shallow water (a threshold of 50 m is used) and on the shore. As can be seen from the figure, anomalous waves have been observed on deep and shallow water (this fact has been examined separately in Ref. [48]). Most frequently, the media's attention is drawn to cases of anomalous waves on the shore (*sneaker waves*), but disasters with sinking ships on the open sea dominate in terms of casualties.

A breakthrough in the recognition of the problem of anomalously high waves by the community of oceanographers and marine engineers is related to the appearance of a large amount of data on instrumental measurement of sea waves. The overwhelming majority of measurements consist of records of displacement at a point obtained by instruments of various types (buoys, altimeters, bottom pressure gauges, etc.) at different depths. In the 21st century, wind waves as high as 30 m have been repeatedly recorded; the significant wave height can reach 14–16 m in the North Atlantic [49, 50] and even higher in other regions [51]. Some waves with exceptionally high levels relative to background waves have

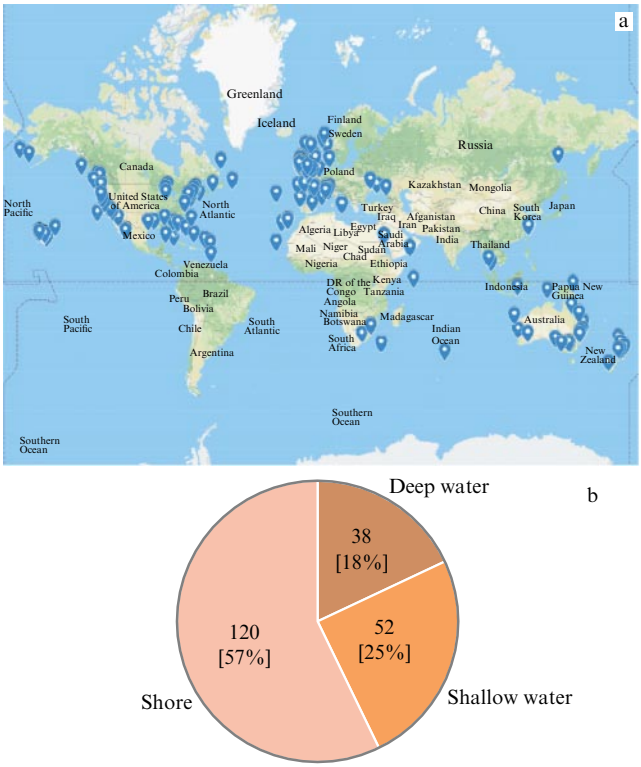

Figure 2. (a) Locations of rogue wave events by reports in the media in 2011–2018. (b) Their distribution over places of occurrence [10].

been given individual names: in addition to the New Year Wave (or the Draupner wave, 1995, AI ≈ 2.24), these include the waves Yura (1987, AI ≈ 2.67), Andrea (2007, AI ≈ 2.67), and Killard (2014, AI ≈ 2.29). The accumulated data of surface wave registration allow retrieving quantitative characteristics of rogue waves and constructing the corresponding probability distributions required in engineering.

Reference [52] presents the results of the processing of 122 million individual waves measured from off-shore platforms and buoys at four different geographical locations (more than 30 measurement points with depths ranging from 7 m to 1.3 km); more than 3.5 thousand of these waves satisfy the amplitude criterion on rogue waves (3). Thus, approximately one wave in 33 thousand turns out to be anomalously high, and if the characteristic period of wind waves is taken as 10 s, it follows that a rogue wave appears once every four days on average. In the database considered, the maximum wave height is 25.5 m and the maximum crest height is 18.5 m. The authors of [52] were not able to identify wave conditions that facilitate the occurrence of rogue waves; anomalous waves are encountered for different combinations of wind waves and swell. The paper concluded that the rogue waves are the result of dispersive focusing, so that no nonlinear mechanisms are needed to explain them.

Another databank based on two decades of records from 34 buoys in the Pacific Ocean is analyzed in Ref. [53]; it contains about 800 million individual waves, including 8 thousand rogue waves (one rogue wave for every 100 thousand waves). It is mentioned that the number of rogue waves recorded by a buoy per year may reach 50. No significant connection was found between the frequency of rogue waves and sea depth (measurements were carried out in conditions of relatively deep water, more than 80 m). During the whole observation period, the amplification index AI (3) reached the value of 3 five times.

The dependence between the occurrence frequency and the recording location was investigated in Ref. [54] by processing the records from 80 buoys located along the American coasts for depths of 10 m or more, containing 1.1 billion individual waves and almost 75 thousand rogue waves with AI > 2, including 19 waves with AI > 5; on average, there is one rogue wave for every 15 thousand waves. (According to the Raleigh statistics (2), the amplification AI $= 5$ should correspond to the event repetition once in 10^{15} years for waves with a period of 10 s. This result indicates that either the probability of the occurrence of rogue waves is in fact much higher or the measurements are not reliable.) As emphasized in that study, the sensitivity to local conditions is particularly high in coastal regions, and it is most likely that the mechanisms for rogue wave formation differ between locations. Multi-year observations in [55] also reveal interannual variability in the frequency of rogue wave occurrence, which manifests itself differently at different sites in the world's oceans.

More than 300 million individual waves measured by different gauges in the conditions of the shallow North Sea (not deeper than 35 m) were analyzed in Ref. [56]. In comparison with the cases described above, they demonstrate a higher mean frequency for the occurrence of rogue waves — once in 5–8 thousand waves, depending on the observation point. Reference [44], based on a statistical study of more than 1 million waves recorded by buoys at different depths concludes that rogue waves occur more frequently under conditions of open sea and deep water.

We note that the above estimate for the mean recurrence rate of anomalously high waves are substantially lower than follows from linear theory for a narrow-band Gaussian process — the Rayleigh curve (2) (one rogue wave in 3000). It also contradicts the results of earlier field studies [57–59], which reported a significant underestimation of rogue wave probability by the Rayleigh distribution.

A fundamental difficulty in obtaining probability distributions based on field measurements lies in the statistical inhomogeneity and finiteness of the samples (*sampling variability*). In addition, there is the question of the quality of the registration of anomalous waves, which is related to the accuracy of the procedure used to reconstruct the surface displacement information in the case of indirect measurement (by a bottom pressure gauge, an accelerometer on a buoy, etc.), as well as to the technical details of instruments and errors associated with them. Empirical procedures applied during wave registration for data quality control may themselves be a source of systematic errors. The contradictory conclusions drawn from the statistical processing of long-term field measurement data discussed above place particular importance on the results of physical modeling by direct numerical simulations or experimental measurements under controlled conditions.

In addition to estimating the probability properties of anomalous waves, the data from field measurements are examined with respect to characteristic forms of such waves, which can be used, for example, to estimate loads on constructions. A special form of anomalous wave occurring in the strong countercurrent at Cape Agulhas (south-west African coast) has already been mentioned in the literature, with a long sloping trough preceding a steep high crest, the so-called Lavrenov wave [60].

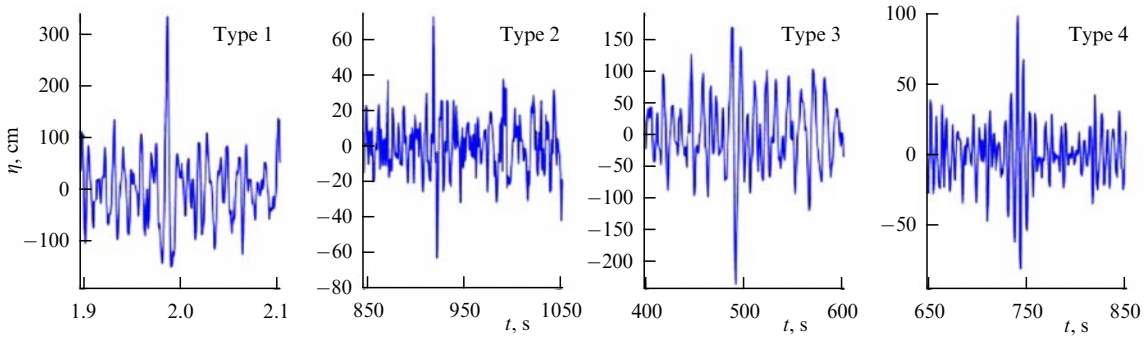

Figure 3. Different forms of rogue waves recorded by a buoy on the western shelf of India [61]: high crest (type 1), changing sign wave (type 2), 'hole in sea' (type 3), and intense group (type 4).

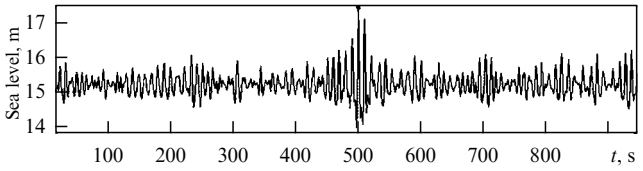

Figure 4. Record of waves in the region of the mouth of Lake Izmenchivoe (Sakhalin) containing an anomalous wave with AI = 2.65 [63].

Overall, the observational data reveal a diversity of rogue wave shapes, even when measured at the same location at different times. Figure 3 shows the shapes of rogue waves found in records from a buoy deployed at 13 m depth off the western Indian coast [61]. The most common anomalously high waves are single waves with a large crest (type 1); they can be of variable sign (type 2), but can also occur within a group of several large waves (the 'ninth wave' or 'tenth wave' or 'three sisters', type 4). Waves with a very deep trough (the so-called 'hole in the sea', type 3) have also been recorded, and in the study reported in Ref. [61], holes in the sea accounted for 40% of the total number of rogue waves. In observational results in the coastal zone of the Baltic Sea [62], 63% of the rogue waves were the single crest type and 17% the single trough type. Most of the anomalous waves in the shallow part of the Sakhalin shelf were represented by groups of high waves, as in the example shown in Fig. 4. Rogue waves were also recorded in the Black Sea [4, 64].

Rigorous statistical studies of anomalous wave shapes with good significance are rare. Averaged profiles of observed rogue waves, based on the results of two studies, are shown in Fig. 5; they look quite similar. Reference [52] mentions a higher mean steepness of rogue waves than of 'normal' large waves (Fig. 5a). As can be seen, the wave crests are sharper, and their height is greater than the depression in nearby troughs, which is qualitatively consistent with the solution for a stationary nonlinear wave on deep water (the Stokes wave). Some of the records of rogue waves (e.g., the Andrea Wave) show a strong crest asymmetry, which is an indicator of breaking. Averaged profiles of extreme waves for given AI thresholds were constructed in Ref. [54] and compared with the shapes of 'normal' waves (AI < 2) and also with the conclusions of other studies based on field data. Although the authors of studies mentioned here agree on the conclusion that the characteristic portrait of a rogue wave includes a sharp crest moving between shallower troughs, the conclusions regarding a more detailed description are ambiguous. Figure 5b from Ref. [54] shows profiles of extreme waves which look noticeably different for the sets of rogue waves

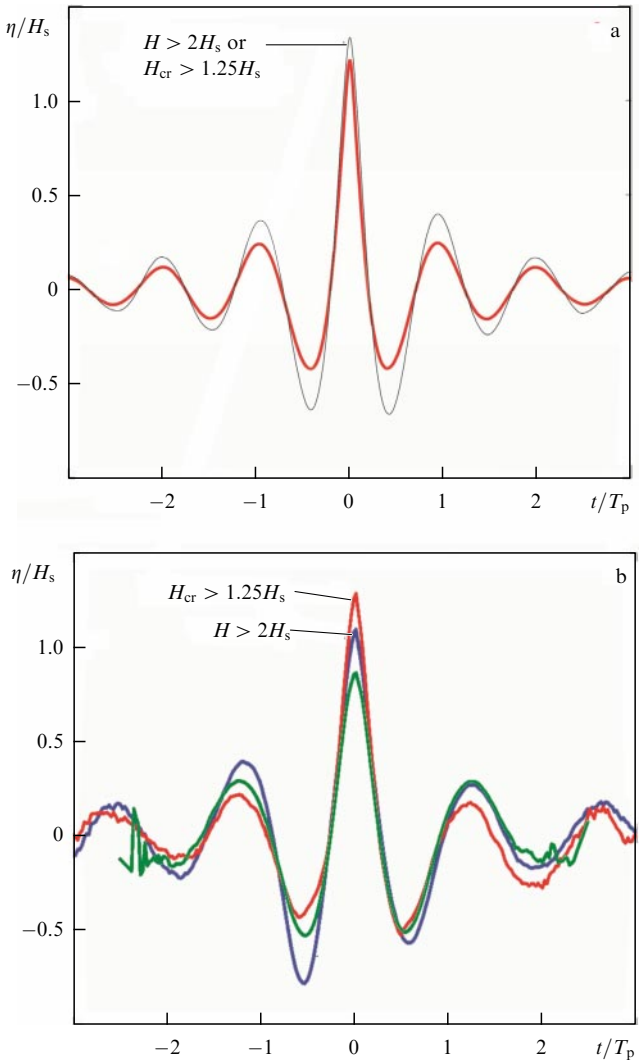

Figure 5. (a) Mean rogue wave profile (black curve) and 1% of 'normal' waves with a maximum crest amplitude (red curve) based on the results of Ref. [52]. (b) Form of rogue waves with a height larger than $2H_s$ (blue curve), crest height larger than $1.25H_s$ (red curve) and also 1% of highest 'normal' waves (green curve) based on the results of Ref. [54].

selected by height (3) (blue curve) and an analogous criterion for crest heights (red curve). According to the results of measurements near the Brazilian coast [58], rogue waves with deeper troughs behind the extreme crest are encountered almost twice as often as those with troughs in front. This conclusion is the opposite of the picture in Fig. 5b (blue

curve). Substantial differences in the shape and asymmetry of extreme waves dependending on whether they reach the breaking threshold are discussed in Ref. [65].

In recent years, new approaches for theoretical and experimental oceanography have been developed to describe the motion of a two-dimensional surface, supported by the growing capabilities of direct numerical modeling of sea waves as well as the development of stereometric wave registration methods in natural conditions [66–68]. It is expected that going beyond one-point measurements of the sea surface and observing wave dynamics in time and space will allow more precise answers to be obtained about the shapes of rogue waves, their probability properties, and the most efficient generation mechanisms.

3. Physical mechanisms and models of the occurrence of rogue waves

A proper understanding of physical effects leading to the occurrence of rogue waves is needed to model their dynamics and statistics and to develop forecast methods. In addition to the description of physical mechanisms, we also formulate basic models in Section 3.1.

3.1 Basic hydrodynamic equations

To describe sea waves on scales that we are interested in, the assumption that fluid motion is potential is commonly very reliable, leading to Laplace's equation for the velocity potential $\varphi(x, y, z, t)$, which will be written for a homogeneous layer of incompressible water above the horizontal bottom $z = -h$ and with free surface $z = \eta(x, y, t)$:

$$\frac{\partial^2\varphi}{\partial x^2} + \frac{\partial^2\varphi}{\partial y^2} + \frac{\partial^2\varphi}{\partial z^2} = 0\,, \quad -h \leqslant z \leqslant \eta\,. \tag{5}$$

A Cartesian reference frame (x, y, z) is used, with the z-axis directed vertically upward and the x direction selected each time to be aligned with the dominant direction of wave propagation. The system of hydrodynamic equations also includes the condition of impermeable bottom and kinematic and dynamical conditions on the free surface [26, 69]:

$$\frac{\partial\varphi}{\partial z} = 0\,, \quad z = -h\,, \tag{6}$$

$$\frac{\partial\eta}{\partial t} = -\frac{\partial\Phi}{\partial x}\frac{\partial\eta}{\partial x} - \frac{\partial\Phi}{\partial y}\frac{\partial\eta}{\partial y} + \left[1 + \left(\frac{\partial\eta}{\partial x}\right)^2 + \left(\frac{\partial\eta}{\partial y}\right)^2\right]\frac{\partial\varphi}{\partial z}\,, \quad z = \eta\,, \tag{7}$$

$$\frac{\partial\Phi}{\partial t} = -g\eta - \frac{1}{2}\left(\frac{\partial\Phi}{\partial x}\right)^2 - \frac{1}{2}\left(\frac{\partial\Phi}{\partial y}\right)^2 + \frac{1}{2}\left(\frac{\partial\varphi}{\partial z}\right)^2 \times \left[1 + \left(\frac{\partial\eta}{\partial x}\right)^2 + \left(\frac{\partial\eta}{\partial y}\right)^2\right] - P_{\mathrm{a}}\,, \quad z = \eta\,. \tag{8}$$

In (7) and (8), the surface potential $\Phi(x, y, t) = \varphi(x, y, z = \eta, t)$ is introduced, g is the acceleration due to gravity, and P_{a} is the atmospheric surface pressure. In the problems considered here, surface tension can be ignored for waves longer than 10 cm. Ignoring weak effects due to the inhomogeneity of pressure P_{a}, without loss of generality, one can take $P_{\mathrm{a}} \equiv 0$, in which case equations (5)–(8) describe only the motion of water.

In the approximation of small-amplitude waves, the solution of equations (5)–(8) takes the form [69]

$$\eta(\mathbf{x}, t) = \mathrm{Re}\left[A\exp(\mathrm{i}\theta)\right]\,, \quad \theta = \mathbf{k}\mathbf{x} - \omega t\,, \tag{9}$$

$$\varphi(\mathbf{x}, z, t) = \frac{g}{\omega}\,\mathrm{Im}\left[A\exp(\mathrm{i}\theta)\right]\Psi(z)\,,$$

$$\Psi(z) = \frac{\cosh\left(|k|(z+h)\right)}{\cosh\left(|\mathbf{k}|h\right)}\,, \tag{10}$$

$$\omega(\mathbf{k}) = \sqrt{g|\mathbf{k}|\tanh\left(|\mathbf{k}|h\right)}\,. \tag{11}$$

Here, the notation $\mathbf{x} = (x, y)$ is introduced for the vector lying in the horizontal plane, the parameter $\mathbf{k} = (k_x, k_y)$ is the wave vector, ω is the cyclic frequency linked to the wave vector through the dispersion relation (11), and A is the wave amplitude. The vertical structure of the velocity potential enters (10) as a factor $\Psi(z)$ which depends on the wave number. A general solution to the initial problem is presented in the form of the integral of (9)–(11) over the wave vectors (a presentation in the form of the Fourier integral).

Surface waves can be efficiently described using the Hamiltonian formalism developed in Ref. [26]. The variables η and Φ form a canonical pair with the Hamiltonian H, and motion equations for them take the form

$$\frac{\partial\eta}{\partial t} = \frac{\delta H}{\delta\Phi}\,, \quad \frac{\partial\Phi}{\partial t} = -\frac{\delta H}{\delta\eta}\,, \tag{12}$$

$$H = T + U\,, \quad T = \frac{1}{2}\int \mathrm{d}\mathbf{x}\int_{-h}^{\eta}(\nabla\varphi)^2\,\mathrm{d}\mathbf{z}\,,$$

$$U = \frac{g}{2}\int \eta^2\,\mathrm{d}\mathbf{x}\,. \tag{13}$$

The introduction of normal variables $a_{\mathbf{k}}(t)$ in the two-dimensional space of wave vectors allows one to obtain nonlinear equations in a spectral form:

$$\frac{\partial a_{\mathbf{k}}}{\partial t} = -\mathrm{i}\frac{\delta H}{\delta a_{\mathbf{k}}^*}\,, \tag{14}$$

$$\eta_{\mathrm{k}} = \sqrt{\frac{\omega_{\mathbf{k}}}{2g}}\left(a_{\mathbf{k}} + a_{-\mathbf{k}}^*\right)\,, \quad \Phi_{\mathbf{k}} = -\mathrm{i}\sqrt{\frac{g}{2\omega_{\mathbf{k}}}}\left(a_{\mathbf{k}} - a_{-\mathbf{k}}^*\right)\,,$$

$$a_{\mathbf{k}} = \frac{1}{2\pi}\int a(\mathbf{x}, t)\exp(-\mathrm{i}\mathbf{k}\mathbf{x})\,\mathrm{d}\mathbf{x}\,, \tag{15}$$

where $\eta_{\mathbf{k}}$ and $\Phi_{\mathbf{k}}$ are the Fourier transforms of the surface displacement and surface potential, respectively, and $\omega_{\mathbf{k}} = \omega(\mathbf{k})$ is the dispersion relation for linear waves. The Hamiltonian of interaction between waves H_{int} ($H = H_0 + H_{\mathrm{int}}$, $H_0 = \int\omega_{\mathbf{k}}a_{\mathbf{k}}a_{\mathbf{k}}^*\,\mathrm{d}\mathbf{k}$) has a complex form. Its representation as an asymptotic expansion in a small parameter of wave steepness allows one to obtain simpler approximate equations [70–72]. The transform to new canonical variables $b_{\mathbf{k}}(t)$ excludes nonresonant three-wave interactions from dynamical equations and simplifies the nonlinear part. The resulting evolution equation for waves on deep water in new variables preserves the form (14),

$$\mathrm{i}\frac{\partial b_{\mathbf{k}}}{\partial t} = \omega_{\mathbf{k}}b_{\mathbf{k}} + \int T_{\mathbf{k}\mathbf{k}_1\mathbf{k}_2\mathbf{k}_3}b_{\mathbf{k}_1}^*b_{\mathbf{k}_2}b_{\mathbf{k}_3} \times \delta(\mathbf{k} + \mathbf{k}_1 - \mathbf{k}_2 - \mathbf{k}_3)\,\mathrm{d}\mathbf{k}_1\,\mathrm{d}\mathbf{k}_2\,\mathrm{d}\mathbf{k}_3\,. \tag{16}$$

The Zakharov equation (16) remains technically difficult to solve because of the six-dimensional integral on the right-hand side. The nonlinear coefficient of four-wave interactions $T_{\mathbf{k}\mathbf{k}_1\mathbf{k}_2\mathbf{k}_3}$ in the integrand also has a rather cumbersome form [70], but possesses symmetry over the indices of interacting waves and also homogeneity, which can be used (see Section 5.2).

3.2 Geometrical and dispersive focusing

To describe wave focusing, also in the conditions of a smoothly varying medium, for example, for variable depth, a convenient approximation is that of geometrical optics [69]. Rays along which a linear wave described by (9)–(11) is propagating are defined by the system in the Hamiltonian form

$$\frac{\mathrm{d}\mathbf{x}}{\mathrm{d}t} = \frac{\partial\omega}{\partial\mathbf{k}}\,, \quad \frac{\mathrm{d}\mathbf{k}}{\mathrm{d}t} = -\frac{\partial\omega}{\partial\mathbf{x}}\,, \tag{17}$$

where the wave vector and frequency, which are functions of coordinates and time, are defined through the wave phase $\theta(\mathbf{x}, t)$: $\mathbf{k}(\mathbf{x}, t) = \nabla\theta$, $\omega(\mathbf{x}, t) = -\partial\theta/\partial t$. Under the same assumptions, the wave amplitude is found from the energy balance equation

$$\frac{\partial|A|^2}{\partial t} + \nabla\left(\mathbf{c}_{\mathrm{gr}}|A|^2\right) = 0\,, \tag{18}$$

where $\mathbf{c}_{\mathrm{gr}} = \partial\omega/\partial\mathbf{k}$ is the group velocity. The wave amplitude increases in regions of the convergence of rays along which energy is transferred (the effect of geometrical focusing). Such a situation can occur when different wave systems interfere with one another (for example wind waves generated by different storms), when waves are refracted by the characteristic properties of bathymetry (submarine hills, ridges, coastlines and so on), and in currents.

Ray theory is developed very well in physics, in particular as applied to waves on the water surface (for example, tsunami waves). The wave amplitude in caustics, formally tending to infinity, proves to be finite under a more accurate analysis. The pattern of rays, caustics, and regions of wave energy focusing is very complex and variable in conditions of the real ocean and can be viewed as random.

Dispersive focusing is another obvious linear mechanism for the generation of large amplitude waves. It can be described with the help of a Fourier transform based on the solution (9)–(11), but becomes more transparent after the reduction of (17) to the kinematic equation for the group velocity $c_{\mathrm{gr}}(k)$ (here, for simplicity, we consider unidirectional motion, $\mathbf{c}_{\mathrm{gr}} = (c_{\mathrm{gr}}, 0)$) [73]:

$$\frac{\partial c_{\mathrm{gr}}}{\partial t} + c_{\mathrm{gr}}\,\frac{\partial c_{\mathrm{gr}}}{\partial x} = 0\,. \tag{19}$$

The solution of equation (19) takes the form of simple wave $c_{\mathrm{gr}}(x, t) = c_0(x - c_{\mathrm{gr}}t)$ and can be analyzed graphically. At the initial time moment $t = 0$, faster waves are behind the slow one in the wave train if $\mathrm{d}c_0/\mathrm{d}x < 0$. Thus, the wave energy will be summed in these intervals of the wave train, which corresponds to an increase in the instantaneous gradient of function $c_{\mathrm{gr}}(x)$. The evolution of wave intensity is described by the one-dimensional version of equation (18), the solution of which in the form of a Riemann wave can be found analytically and may reach formally an infinite value upon summing waves with different wavelengths.

Wind-generated waves can be quite inhomogeneous in both direction and wavelength, creating conditions for ongoing processes of random spatio-temporal focusing [74]. At the same time, random wave superposition is taken into account in the framework of Gaussian statistics and the resulting Rayleigh distribution for wave heights, so that the events of geometric and dispersive focusing in homogeneous stationary conditions do not alter the Rayleigh probability distribution for extreme waves.

Processes of linear superposition of waves with different wavelengths or directions have been repeatedly reproduced in different variants under laboratory conditions and can be considered to be standard [75, 76]. The consideration of a nonlinear correction to frequency (the so-called nonlinear dispersion relation) improves the description, but complicates the problem of finding the wave train that provides the most efficient focusing. An efficient method here is the wavefront inversion method, where a nonlinear initial value problem is solved with the expected form of the rogue wave, and the solution obtained at a large time is then inverted to perform a process backward in time [73, 77, 78]. From a physical point of view, the focusing of linear and nonlinear wave trains proceeds in the same way in the absence of instabilities; hence, dispersion focusing is also mentioned in the framework of nonlinear problems. The effects of dispersive and geometric wave convergence may govern the initial phase of wave growth, which is then continued further as a result of the action of nonlinear mechanisms [79–81].

3.3 Nonlinear wave interactions and modulation instability

Nonlinearity violates the independence of spectral components assumed by the central limit theorem, which can lead to significant deviations from the Gaussian statistics. The effects of nonlinearity determine the dynamics of large waves and are therefore of primary importance for the description of realistic rogue waves. As the solution to the nonlinear problem is complicated, a significant part of the research is based on numerical modeling and/or approximate equations.

The dominant part of the research is concerned with the conditions of the open ocean and large depths ($kh \gg 1$), when the dispersion is strong. For deep water waves, the resonance conditions between wave triplets (quadratic nonlinearity) do not hold in typical situations, and the nonlinear dynamics are driven by the next order nonlinearity (4-wave interactions). Nonresonant quadratic and higher-order interactions are explicitly manifested in the deviation of the waveform from sinusoidal, but do not affect the evolution of the spectra of normal waves $b_{\mathbf{k}}$ (16). The conditions for 4-wave resonance interaction are written as

$$\mathbf{k}_1 + \mathbf{k}_2 = \mathbf{k}_3 + \mathbf{k}_4\,, \quad \omega_1 + \omega_2 = \omega_3 + \omega_4\,, \tag{20}$$

where each of frequencies is determined from the dispersion relation $\omega_j = \omega(\mathbf{k}_j)$, $j = 1, 2, 3, 4$. The resonance conditions are written for the limit of waves with infinitesimal amplitude, although they are modified under the action of nonlinearity. It has been repeatedly shown that quasi-resonance (near resonance) interactions play no smaller a role than the interactions between waves in exact resonance [82, 83]. In the case of waves on deep water, the degree of nonlinearity is characterized by the wave steepness $\varepsilon \sim k|A|$.

The expression for the surface displacement excess kurtosis, which takes into account weak correlations of normal waves as the result of 4-wave interactions in the

framework of the Zakharov equations, can be found in Ref. [84],

$$\lambda_4^{\rm dyn} = \frac{12}{g^2\sigma^2}\int T_{\mathbf{kk_1k_2k_3}}\sqrt{\omega\omega_1\omega_2\omega_3}\,G_r N_1 N_2 N_3 \times \delta(\mathbf{k}+\mathbf{k_1}-\mathbf{k_2}-\mathbf{k_3})\,{\rm d}\mathbf{k}_1{\rm d}\mathbf{k}_2{\rm d}\mathbf{k}_3\,, \quad (21)$$
$$\langle bb_1^*\rangle = N(\mathbf{k})\,\delta(\mathbf{k}-\mathbf{k}_1)\,, \quad G_r = \frac{1-\cos(\Delta\omega t)}{\Delta\omega}\,,$$

where

$$\Delta\omega = \omega+\omega_1-\omega_2-\omega_3\,.$$

Relationship (21) is written for spectral components of wave action $N(\mathbf{k})$ (angular brackets imply ensemble averaging), and thus does not contain the wave phase dependences, but inherits the six-dimensional integration from the dynamical equation. This integral is computed in Ref. [85] for quasistationary conditions (large time t) under the assumption of a narrowband spectrum:

$$\lambda_4^{\rm dyn} = \frac{\pi}{\sqrt{3}}\,{\rm BFI}^2\,, \quad (22)$$

where the parameter BFI (Benjamin–Feir Index) is computed through the ratio of the measures of wave nonlinearity to dispersion,

$${\rm BFI} = \sqrt{2}\,\frac{\varepsilon}{\delta_k}\,. \quad (23)$$

Here, $\delta_k = \Delta k/k$ is the relative width of the wavenumber spectrum. The full excess kurtosis in (4) is composed of the dynamic one $\lambda_4^{\rm dyn}$ and the contribution defined by nonresonant interactions $\lambda_4^{\rm bound}$ (bound nonlinear waves),

$$\lambda_4 = 3+\lambda_4^{\rm dyn}+\lambda_4^{\rm bound}\,, \quad \lambda_4^{\rm bound} = 24\varepsilon^2\,. \quad (24)$$

In the framework of the weakly nonlinear theory of second order $O(\varepsilon^2)$, the skewness is set by bound waves, $\lambda_3 = 3\varepsilon$. For a real sea, the estimate $\varepsilon = k\sigma = 0.03-0.1$ for mean steepness can be used; therefore, the skewness and excess kurtosis from bound waves are small. The BFI parameter is not necessarily small if wave steepness is large or the wavenumber spectrum is sufficiently narrowband, in which case the net excess kurtosis can increase considerably because of its dynamical part.

Reference [85] shows theoretically that for a weakly non-Gaussian process the increase in the fourth moment, $\lambda_4 > 3$, leads to an increase in the probability of waves with large height, $H > 4\sigma$,

$$P(H) \approx \exp\left(-\frac{H^2}{8\sigma^2}\right)\left[1+(\lambda_4-3)B\left(\frac{H}{\sigma}\right)\right],$$
$$B(\xi) = \frac{1}{384}\,\xi^2(\xi^2-16) \quad (25)$$

(the Gram–Charlie series for a weakly non-Gaussian distribution [25]); for this reason, the excess kurtosis is frequently used as an index indicating the degree to which the sea waves are anomalous.

The BFI (23), which corresponds to the similarity parameter of the nonlinear Schrödinger equation, was proposed in Refs [84, 86] as a deep-water analog of the known Ursell parameter for weakly nonlinear weakly dispersive waves on shallow water. Based on this understanding, the BFI parameter for a finite sea depth can be readily written taking into account the coefficients of NSE (see Section 5.2, equation (61))—the nonlinearity α and dispersion β: ${\rm BFI}_{\rm finite\ depth} = {\rm BFI}(\alpha/\beta)^{1/2}$ [87].

The criterion ${\rm BFI} > 1$ corresponds to the condition for the occurrence of modulational wave instability (see review [27]). Instability of uniform waves with respect to sufficiently long perturbations develops as a result of quasi-resonant 4-wave nonlinear interactions and is a dominant type of instability for waves of small and moderate steepness on deep water [88]. Longitudinal perturbations of nonlinear waves gain stability if the depth decreases, $kh < 1.363$; in contrast, perturbations at an angle to the direction of wave propagation remain unstable, but with a smaller increment down to depths $kh \sim 0.5$. Modulational instability disappears at smaller depths.

We note that, in fact, the BFI parameter was discussed much earlier by I Alber [89], who proposed an analog of NSE to describe random waves. Based on estimates made, Alber concluded that typical sea wave spectra correspond to the stability condition, although they are close to the instability threshold. He formulated a hypothesis that modulational instability prohibits the development of conditions with too narrow a spectrum. Today, the effect of modulational instability of sea waves is considered a mechanism for the formation of large amplitude waves, increasing their probability. A mathematical description of these processes in the framework of approximate integrable models is discussed in Section 4. The important role of strong nonlinearity effects, leading to a sharper growth of anomalous wave and subsequent breaking, was stressed in Ref. [90]. We note that Ref. [91] drew attention to nonlinear effects of 5-wave interactions. Its authors observed their manifestations in the spectrum of the New Year Wave record. Five-wave resonances are realized only for three-dimensional waves, which complicates their study.

3.4 Generalizations of modulation instability parameter

The index of modulation instability, BFI (23), introduced theoretically using a set of assumptions, is written for the spectrum parameters ε and δ_k, so that it hypothetically allows one to estimate the danger of a sea state based on the standard output data of existing (spectral) models forecasting sea waves. A set of studies sought the form of the expression for this index defining the modulation instability threshold in conditions more realistic for a sea.

Longitudinal perturbations of waves on deep water correspond to the maximum increment of modulation instability [88], whereas perturbations at too large an angle to the dominant wave propagation direction are stable. To describe directional random waves, several alternative variants of the parameter of modulation instability were proposed in the literature. In Ref. [92], a modification of BFI is formulated based on theoretical ideas about the dependence of excess kurtosis on the parameters of weakly nonlinear waves with a narrowband spectrum, numerical simulation of NSE for two spatial coordinates, and a comparison with the data of laboratory measurements,

$${\rm BFI}_{\rm 2D}^2 = \frac{{\rm BFI}^2}{1+\alpha_2 R}\,, \quad R = \frac{\delta_\theta^2}{2\delta_\omega^2}\,. \quad (26)$$

Here, $\delta_\omega = \delta_k/2$ is the relative width of the frequency spectrum for waves on deep water, δ_θ is the relative width of the angular spectrum, and $\alpha_2 = 7.1$ is an empirical coefficient. In such a representation, the formula for dynamic kurtosis

(22) preserves its form: only the BFI parameter should be replaced by its two-dimensional analog $\mathrm{BFI}_{2\mathrm{D}}$. A similar representation based on the modification of the formula for spectral bandwidth was used in Ref. [93].

Other alternatives to the BFI were proposed in Refs [94, 95] on the basis of the already mentioned Alber equations. In Ref. [94], a factor depending on the width of the angular spectrum was added to definition (23). Reference [95] used the model sea wave spectrum JONSWAP [96] in an explicit form (see Section 5) and proposed new parameters in the form

$$\Pi_1 = \frac{\varepsilon}{\alpha_{\mathrm{P}}\gamma}\,, \quad \Pi_2 = \Pi_1 + \frac{0.0256}{\varepsilon A_{\mathrm{d}}}\,, \tag{27}$$

where α_{P} is the multiplier at the spectrum profile, setting the wave intensity (the so-called Phillips parameter) and γ is the peak enhancement factor (the degree to which the main spectral peak is expressed). By default, $\alpha_{\mathrm{P}} \sim 0.01$ and $\gamma = 3.3$. The authors insist that the parameter Π_1 introduced for unidirectional waves is essentially different from BFI (23), since the parameter α_{P} and γ influence the wave steepness as well as spectral width, being physically more adequate characteristics of the spectrum. The same work also proposes a generalization of the modulational instability index for directional waves Π_2. A finite width of the angular spectrum is accounted for in Π_2 (27) with the help of the so-called directional spectral depth A_{d}, $\delta_\theta \sim A_{\mathrm{d}}^{-1}$. Also, Ref. [95] gives estimates of threshold values which correspond to modulation-unstable spectra: $\Pi_1 > 1$ and $\Pi_2 > 1.1$; these values were made more precise by other authors later.

3.5 Coherent wave structures and their interactions

Under the assumption that nonlinear effects are weak, and also that frequency and wavenumber spectra are narrowband, system (5)–(8) can be reduced to simpler nonlinear equations (see also Section 5.2), including those that are integrable using the inverse scattering transform (IST): the Korteweg–de Vries and Kadomtsev–Petviashvili equations (when the wavelength exceeds the depth, $kh \ll 1$) or the nonlinear Schrödinger equation for weak wave modulation. All the listed equations allow exact solutions in the form of structurally stable solitary waves or wave groups which exist owing to the balance between the effects on nonlinearity and dispersion. In the case of waves on deep water, the modulational instability is connected with the breather solutions of the NSE (see Section 4), which, in turn, could be interpreted as envelope solitons on the background of a uniform wave. The existence of solitons is supported by the coherent dynamics of the respective spectral components; therefore, the presence of solitons in irregular wave fields modifies the statistics. It is known that the probability of high waves occurring on shallow and deep water increases if the contribution from the soliton part increases [86, 97]. Soliton interactions may provide principally nonlinear mechanisms of rogue wave generation [98–100]. The interaction of solitary wave groups which propagate at a small angle to each other was proposed as a natural mechanism for the occurrence of rogue waves [101].

In the limiting case when waves are presented exclusively by solitons, we are talking about a soliton gas. The spectrum of the associated scattering problem for integrable equations contains key information on the wave composition. The problem of establishing a link between such a 'nonlinear spectrum' and the statistical properties of the soliton gas (the description of integrable turbulence) is a subject of active research [102–107] which is outside the scope of this review. We only note that different types of soliton gas may provide both increased or reduced probability for rogue waves to appear [103]. A set of studies was carried out on modeling the gas of solitons and envelope solitons in the framework of nonintegrable generalizations of model equations and primitive equations of fluid dynamics [108–110] (see also Section 5.5).

3.6 Nonlinear wave dynamics under varying conditions

Numerous experimental and numerical studies indicate that a modulationally unstable wave system comes to a quasi-equilibrium state. In this process, the wave spectrum sharply broadens at first, and the probability of extreme waves substantially increases; the spectrum then narrows, but to a smaller degree (see Section 5.3). An elegant theoretical rationale for the link between the spectral width and kurtosis is given in Ref. [111] relying on the Hamiltonian representation for the NSE,

$$\lambda_4(t) = \lambda_4(t_0) + \frac{\beta}{2\alpha}\,\frac{\delta_k^2(t) - \delta_k^2(t_0)}{\sigma^2}\,. \tag{28}$$

Here, α and β are, respectively, the coefficients of nonlinearity and dispersion of the NSE (see equation (61) in Section 5.2); the same study also gives a formula for directional waves.

The evolution of excess kurtosis in time under the assumption of weakly non-Gaussian statistics was explored in theoretical studies [112, 113], where the six-dimensional integral (21) needed for computations of the dynamical excess kurtosis is reduced after some assumptions to the form [85, 113]

$$\lambda_4^{\mathrm{dyn}}(t) = 3J(R,\tau)\,\mathrm{BFI}^2\,, \quad \tau = \delta_\omega^2\omega_0 t\,. \tag{29}$$

Here, J is the integral function with cubical dependence on the wave spectrum, τ is the function of time defining the qualitative form of the dependence of J on time, and R is the characteristic of the width of the angular spectrum (26). It was shown that nonlinear self-modulation develops for a sufficiently narrowband spectrum, $R < 1$, in which case the dynamical excess kurtosis at first increases, reaches its local maximum, and then decays, but to a smaller degree.

A similar fast evolution of spectra and wave probability characteristics arises in different situations when a nonlinear wave system becomes unstable to modulation or is subjected to perturbations, if initial conditions are given in the form of a linear superposition of waves with a sufficiently narrowband spectrum [114], for forced reshuffling of wave phases [115], on switching on or off the forcing which is modeling the wind action [116–118]. Analogous behavior was observed when ambient current conditions [119, 120] or local depth [121–123] abruptly changed.

The last case — with a variable depth — attracted special attention because of its importance for coastal regions. The problem of wave transformation over a variable bottom has a long history (linear transformation, propagation of solitons of long waves), but over recent years the focus has been on nonlinear irregular waves and a larger depth range. It is known that, in the case of an adiabatically slow decrease in depth, the solitons of long waves grow faster than linear waves (the nonlinear and linear Green laws, respectively). Qualitatively similar effects are also realized for envelope solitons propagating in nonhomogeneous conditions or under external action [118, 124, 125].

The effect of growth on skewness, kurtosis, and the probability of high waves accompanying fast depth reduction was discovered in numerical and laboratory experiments relatively long ago [121–123]. Solving this problem in a general form presents a difficult task because of the large number of governing parameters and the dependence of nonlinear and dispersive wave properties on depth [126–128]. In the recent study [129], the effect whereby waves become more anomalous when passing through an abrupt depth reduction is explained in the framework of weakly nonlinear second-order theory. The abrupt change in depth destroys the balance between free and bound wave components, which leads to the appearance of new free waves (in particular, half as long) in anti-phase with the parent nonlinear waves. Further wave evolution leads to constructive interference.

A nonlinear mechanism of wave amplification past a sharp increase in depth, proposed in Ref. [125], is linked to the transformation of envelope solitons, which can propagate on not too shallow water, $kh > 1.363$, including the generation of new envelope solitons and their interaction. The proposed mechanism is potentially applicable to any situation where the characteristics of nonlinearity and dispersion vary so that the effective BFI increases. For example, it is applicable when an opposing current becomes stronger, as proposed in Ref. [120].

3.7 Nonlinear dynamics of trapped waves

Trapping and subsequent blocking of waves by currents, leading to an increase in wave amplitudes in certain regions, has been discussed in the framework of linear theory since long ago (see, for example, [74, 130, 131]). Later, these effects were reproduced taking into account weak nonlinearity and also in the framework of full nonlinear models [119, 122, 132] (see also review [133]). The new understanding concerns principally nonlinear mechanisms of the occurrence of extreme waves in fields of trapped waves. As follows from direct numerical simulation and is reflected in two-dimensional expressions for the index of modulation instability (26), (27), the effect of nonlinear self-modulation weakens fast with the increase in the angular spectrum width. Waves with narrow angular and frequency spectra, which are not typical of natural conditions, are most strongly susceptible to modulation instability. In the case of wave trapping by jet currents or extended bottom topography features (topographic waves), in particular, a sloping bottom in shallow regions (edge waves), the formation of wave guides with a modal transverse structure takes place. As a result, the dimension of a dynamical system is effectively reduced, the nonlinear dynamics become close to the case of collinear waves, and substantially more favorable conditions for modulation instability are realized which cannot be achieved in usual cases [134, 135].

4. Mathematical models of rogue waves on the background of modulated waves

Studies of wave dynamics in the framework of the NSE of focusing type, describing modulated surface waves in a sufficiently deep basin (see Section 5.2), have received the most attention. In dimensionless variables, the NSE is expressed in the form

$$\mathrm{i}\psi_t + \frac{1}{2}\,\psi_{xx} + |\psi|^2\psi = 0\,. \tag{30}$$

Here, the complex-valued function $\psi(x,t)$ describes wave modulations and the function $|\psi(x,t)|$ defines wave amplitudes. Equation (30) is invariant to scale transformation so that, if the function $\psi(x,t)$ is a solution of (30), then, for arbitrary real number C, the function $C\psi(Cx, C^2t)$ is also a solution.

4.1 Periodic solutions of the nonlinear Schrödinger equation

The NSE (30) has a solution in the form of a uniform wave of constant amplitude

$$\psi(x,t) = \exp(\mathrm{i}t)\,, \tag{31}$$

which can be generalized with the help of a scale transform and arbitrary shift in time t. More complex solutions can be presented as periodic functions of the coordinate,

$$\psi(x,t) = u(x)\exp(\mathrm{i}\omega t)\,. \tag{32}$$

In (32), the parameter ω has the meaning of frequency correction, and $u(x)$ is a periodic envelope profile which satisfies the Lax–Novikov equation of the second order,

$$u'' + 2|u|^2u - 2\omega u = 0\,. \tag{33}$$

Periodic solutions of equation (33) can be expressed in terms of the Jacobi elliptic functions with modulus $k \in (0,1)$. The two simplest periodic solutions with trivial phases are given by the expressions

$$u(x) = \mathrm{dn}\,(x;k)\,, \quad \omega = \frac{1}{2}\,(2-k^2)\,, \tag{34}$$

$$u(x) = k\,\mathrm{cn}\,(x;k)\,, \quad \omega = \frac{1}{2}\,(2k^2-1)\,. \tag{35}$$

The 'dnoidal' solution (34) is strictly positive, whereas the 'cnoidal' solution (35) changes sign. In the limit $k = 1$, both solutions (34) and (35) transform into an envelope soliton:

$$u(x) = \frac{1}{\cosh x}\,, \quad \omega = \frac{1}{2}\,. \tag{36}$$

Other solutions of equation (33) can be constructed in polar coordinate representation, $u(x) = R(x)\exp(\mathrm{i}\Theta(x))$, which, being inserted into (33), leads to the expressions for functions R an Θ',

$$R(x) = \sqrt{b - k^2\mathrm{sn}^2(x;k)}\,, \quad \Theta'(x) = \frac{b(1-b)(b-k^2)}{b-k^2\,\mathrm{sn}^2\,(x;k)}\,,$$
$$\omega = \frac{1}{2}\,(3b-1-k^2)\,, \tag{37}$$

for arbitrary parameters $b \in (k^2,1)$ and $k \in (0,1)$, and $\Theta'(x)$ is the derivative of function $\Theta(x)$. At the boundaries of the admissible values of the parameter, $b = 1$ and $b = k^2$, solution (37) reproduces solutions (34) and (35), respectively. The exact solutions (34)–(37) were explored in the context of modulation instability and rogue waves [136, 137].

Following the definition of rogue waves as appearing out of nowhere and disappearing without a trace on a given background ψ_b, one can give a mathematical definition of this property for function ψ,

$$\max_{x\in\Re}\left|\psi(x,t) - \psi_\mathrm{b}(x - x_\pm, t - t_\pm)\right| \to 0 \quad \text{at} \quad t \to \pm\infty\,, \tag{38}$$

for some real constants $x_\pm$ and $t_\pm$. We define the numerical factor of wave amplification M, similar to (3), as the ratio of the maximal achievable solution amplitude to the maximum amplitude of background,

$$M = \frac{\max\limits_{(x,t)\in\Re^2} \left|\psi(x,t)\right|}{\max\limits_{(x,t)\in\Re^2} \left|\psi_\mathrm{b}(x,t)\right|}\,. \tag{39}$$

As is well known, the NSE (30) is the compatibility condition $\varphi_{xt} = \varphi_{tx}$ of the Lax pair with the spectral parameter $\zeta \in \mathbb{C}$ and complex-valued eigenvectors $\varphi(x,t)$:

$$\varphi_x = U(\psi,\zeta)\varphi, \quad U(\psi,\zeta) = \begin{pmatrix} \zeta & \psi \\ -\psi^* & -\zeta \end{pmatrix}, \tag{40}$$

$$\varphi_t = V(\psi,\zeta)\varphi,$$

$$V(\psi,\zeta) = \mathrm{i}\begin{pmatrix} \zeta^2 + \frac{1}{2}|\psi|^2 & \zeta\psi + \frac{1}{2}\psi_x \\ -\zeta\psi^* + \frac{1}{2}\psi_x^* & -\zeta^2 - \frac{1}{2}|\psi|^2 \end{pmatrix}. \tag{41}$$

Such a representation allows one to obtain analytical results on the description of modulation instability of waves and the processes of rogue wave formation on their background. The equation with a derivative over the coordinate (40) presents the Zakharov–Shabat spectral problem derived in the pioneering paper [138] (it is a particular case of the system by Ablowitz, Kaup, Newell, and Segur (AKNS) [139]).

The Lax equations possess a symmetry such that, if $\varphi = (\varphi_1, \varphi_2)^\mathrm{T}$ is an eigenvector with an eigenvalue ζ, then $\varphi = (\varphi_2^*, -\varphi_1^*)^\mathrm{T}$ is the eigenvector for the eigenvalue $-\zeta^*$. Thus, the eigenvalues of the associated scattering problem (40) appear in the complex plane by symmetric pairs with respect to the imaginary axis.

4.2 Rogue waves on the background of constant amplitude waves (breathers)

It is well known that the NSE solution in the form of uniform wave (31) is unstable to modulation [27]: small perturbations of sufficiently large length grow exponentially. To illustrate this phenomenon, we consider a perturbation of uniform wave (31) in the form

$$\psi(x,t) = \exp(\mathrm{i}t)\left[1 + (u_0 + \mathrm{i}v_0)\exp(\lambda t + \mathrm{i}kx) + (u_0^* + \mathrm{i}v_0^*)\exp(\lambda^* t - \mathrm{i}kx)\right], \tag{42}$$

where $(u_0, v_0) \in \mathbb{C}$ is an eigenvector describing weak perturbations and $k \in \Re$ is the wavenumber. The relationship for constant $\lambda = \lambda(k)$ follows from a linear analysis of solution stability,

$$\lambda^2 = k^2\left(1 - \frac{1}{4}k^2\right). \tag{43}$$

Unstable perturbations with positive values of λ occur for perturbation wavenumbers k in the interval (0, 2). Thus, sufficiently long perturbations are unstable, with the length $L = 2\pi/k > \pi$.

Reference [140] presents a universal picture of the dynamics of localized perturbations of a uniform wave. For a wide class of localized initial perturbations such that the Zakharov–Shabat problem (40) does not have discrete eigenvalues, it is shown that the solution $\psi(x,t)$ consists of two outer unperturbed sectors separated by a wedge-like central domain filled with modulated periodic waves.

The general picture of periodic perturbations of a plane wave was explored in Ref. [141]. The dynamics of one unstable mode were analyzed with the help of the method of finite-zone potentials based on the spectral Zakharov–Shabat problem with periodic boundary conditions. In the simple case of one-zone perturbation, it was shown that the asymptotic solution is described by a breather (see below) with parameters defined by the initial conditions.

As concerns the modulation instability, the question is how a uniform background wave is deformed by the development of unstable modes, and how anomalously high waves emerge, propagate, and disappear. The *breather* solutions considered below model rogue waves.

The rogue wave type NSE solution (38), localized along the x-coordinate, was constructed by D Peregrine [32],

$$\psi_\mathrm{P}(x,t) = \left[1 - \frac{4(1+2\mathrm{i}t)}{1 + 4(x^2+t^2)}\right]\exp(\mathrm{i}t)\,, \tag{44}$$

and solutions periodic in x with the period $L = 2\pi/k > \pi$ were found in Ref. [33],

$$\psi_\mathrm{A}(x,t) = \left[1 - \left(\frac{k}{2}\right)\frac{k^2\cosh(\lambda t) + 2\mathrm{i}\lambda\sinh(\lambda t)}{k\cosh(\lambda t) - \lambda\cos(kx)}\right]\exp(\mathrm{i}t)\,. \tag{45}$$

Here, $k \in (0,2)$ is a free parameter and λ is given by (43). The maximum amplitude of solution (44) is found as $M = |\psi(0,0)| = 3$. Thus, the Peregrine breather provides three-fold amplification relative to the background wave. The coefficient of wave amplification in solution (45), which is commonly referred to as the Akhmediev breather, is given by the relationship

$$M = \left|\psi(0,0)\right| = 1 + 2\sqrt{1 - \frac{k^2}{4}}, \quad k \in (0,2)\,; \tag{46}$$

it monotonically decreases from 3 to 1 on the change in k from 0 to 2. A perturbation with maximum instability increment $\lambda = 1$ at $k = 2^{1/2}$ corresponds to $M = 1 + 2^{1/2} \approx 2.4$.

A breather solution of the NSE describing modulations periodic in time (which is why it does not satisfy the formal criterion (38)) and localized over x was obtained by E A Kuznetsov [31] even earlier,

$$\psi_\mathrm{K}(x,t) = \left[1 - \left(\frac{\kappa}{2}\right)\frac{\kappa^2\cos(\gamma t) + 2\,\mathrm{i}\gamma\sin(\gamma t)}{\gamma\cosh(\kappa x) - \kappa\cos(\gamma t)}\right]\exp(\mathrm{i}t)\,, \tag{47}$$

where $\gamma = \kappa\,(1 + \kappa^2/4)^{1/2}$, and $\kappa \in (0,\infty)$ is a free parameter. The Kuznetsov solution (47) is linked with (45) by the formal transformation $k = \mathrm{i}\kappa$, $\lambda = \mathrm{i}\gamma$. The Peregrine breather can be obtained from (45) and (47) in the limits $k \to 0$ and $\kappa \to 0$, respectively.

Multi-breather solutions were constructed in an analytical form; their simplest forms represent multiply degenerate algebraic Peregrine breathers (high-order breathers or *super-rogue waves*) [35, 142, 143].

As is shown in Ref. [34], solutions (44), (45), and (47) are degenerate cases of a more general class of doubly periodic (in x and t) solutions of the NSE (30) in the form

$$\psi(x,t) = \left[q(x,t) + \mathrm{i}\delta(t)\right]\exp\left(\mathrm{i}\theta(t)\right), \tag{48}$$

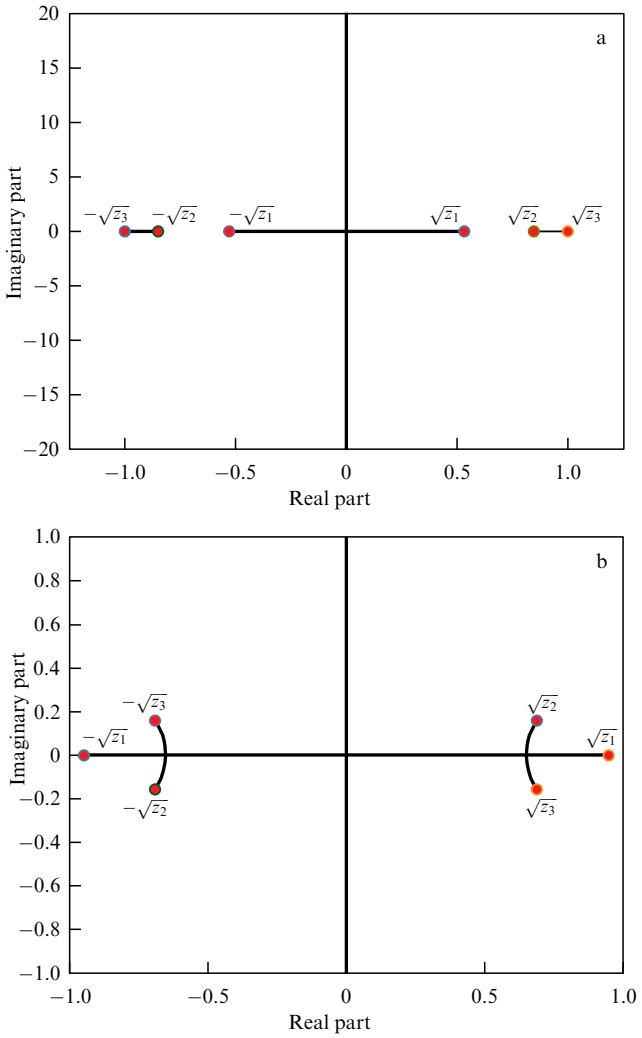

Figure 6. Examples of the scattering problem spectra on the complex plane ζ for doubly periodic solutions (48) [144].

where q, δ, and θ are real-valued functions. For a fixed time moment t, the function $u(x) = q(x,t) + \mathrm{i}\delta(t)$ satisfies the Lax–Novikov equation of the third order,

$$u''' + 6|u|^2 u' - 2\omega u' = 0\,, \tag{49}$$

and doubly periodic solutions are expressed through rational functions which contain the Jacobi elliptic functions (for details, see Ref. [144]).

Figure 6 plots the spectrum of scattering problem (40) for two families of doubly periodic solutions (48). The form of solution depends on three pairs of roots, $\pm\sqrt{z_1}$, $\pm\sqrt{z_2}$, $\pm\sqrt{z_3}$, of the associated polynomial $P(\zeta)$,

$$P(\zeta) = \zeta^6 - \omega\,\zeta^4 + \frac{1}{4}\,(\omega^2 + 8C_1)\,\zeta^2 + C_2 - \omega C_1\,, \tag{50}$$

where ω is the parameter of equation (49), and C_1 and C_2 are the integration constants for this equation (for details, see Ref. [144]). The spectrum in Fig. 6a corresponds to real roots $0 \leqslant z_1 \leqslant z_2 \leqslant z_3$, and the spectrum in Fig. 6b corresponds to one real root, $z_1 > 0$, and two complex conjugate roots, $z_2 = z_3^*$. The roots $\pm\sqrt{z_1}$, $\pm\sqrt{z_2}$, $\pm\sqrt{z_3}$ are indicated by red dots in Fig. 6.

According to the Floquet theory, the spectrum of the scattering problem, which corresponds to solutions periodic in x (48), is composed of regions of the continuous spectrum shown by the black lines in Fig. 6, for which the solutions to the spectral Zakharov–Shabat problem are bounded quasi-periodic functions. In addition to the imaginary axis (which always belongs to the spectrum), the spectrum includes three continuous lines connecting six roots of the polynomial $P(\zeta)$.

When $z_3 = 1, z_1 = z_2 = \zeta_0^2 < 1$, where $\zeta_0 = (1 - k^2/4)^{1/2}$, the gaps between spectral lines on the real axis (Fig. 6a) shrink into a pair of points $\pm\zeta_0$ belonging to the interval $[-1, 1]$. In this limit, solution (48) transforms into the Akhmediev breather (45). When $z_1 = 1$ and $z_2 = z_3 = \zeta_0^2 > 1$, where $\zeta_0 = (1 + \kappa^2/4)^{1/2}$, the outer spectral lines on the real axis (Fig. 6a) contract to a pair of points $\pm\zeta_0$ outside the interval $[-1, 1]$. Such a situation corresponds to the transformation of solution (48) into the Kuznetsov breather (47). The same degeneration takes place when $z_1 = 1$ and the complex spectral lines in Fig. 6b coalesce in a pair of points $\pm\zeta_0$.

If $z_1 = z_2 = z_3 = 1$, all three pairs of roots spawn a pair of points ± 1 at the ends of spectral interval $[-1, 1]$. In this limit, the doubly periodic solution (48) degenerates into the Peregrine breather (44) with a power-law decay in x and t.

Generalized breather solutions for complex eigenvalues $\{\zeta_0, -\zeta_0^*\}$ that were constructed in Refs [145, 146] were discussed in relation to rogue waves; they present perturbations of a background wave moving relative the selected reference system. Pairs of breathers propagating towards each other correspond to quadruplets of eigenvalues $\{\pm\zeta_0, \pm\zeta_0^*\}$; such exact solutions were constructed in Ref. [147].

Recent publications devote great attention to breather stability. The dynamics of the Peregrine and Kuznetsov breathers under the action of perturbations was explored in Refs [148, 149] with the use of IST for functions that decay into nonzero boundary conditions. The completeness of squares of eigenfunctions of the Zakharov–Shabat spectral problem (40) in the class of functions that decay into nonzero boundary conditions was proven in Ref. [150], where this result has been used in the study of the linearized NSE:

$$\mathrm{i}v_t + \frac{1}{2}\,v_{xx} + 2|\psi|^2 v + \psi^2 v^* = 0\,. \tag{51}$$

The linear approximation does not give a description of the transformation of perturbed Peregrine breathers. Reference [151] shows a structural instability of the spectrum of the scattering problem for the Peregrine solution with respect to small perturbations. Depending on the sign of scalar quantity

$$\int_{-\infty}^{\infty} \psi_{\mathrm{P}}(x,0)\left[\mathrm{Re}\left(\psi(x,0)\right) - \psi_{\mathrm{P}}(x,0)\right]\mathrm{d}x\,, \tag{52}$$

where ψ_{P} is the Peregrine solution (44) and $\psi(x,0)$ is the initial condition for NSE (30) satisfying the boundary condition $\psi(x,0) \to 1$ for $|x| \to \infty$, from the end points of spectral interval $[-1, 1]$, either a pair of eigenvalues or a quadruplet is born. The first case corresponds to the emergence of a 'standing' Kuznetsov breather, as shown in Fig. 7a, and in the second case a symmetric pair of breathers is born which are moving in opposite directions (Fig. 7b).

The instability of Peregrine breathers is illustrated in Ref. [152] through numerical simulations of the temporal evolution in the NSE framework. The linear instability of Peregrine breathers was also explored in Ref. [153].

A detailed numerical study of linear stability of Kuznetsov breathers was performed in Ref. [154] with the help of the

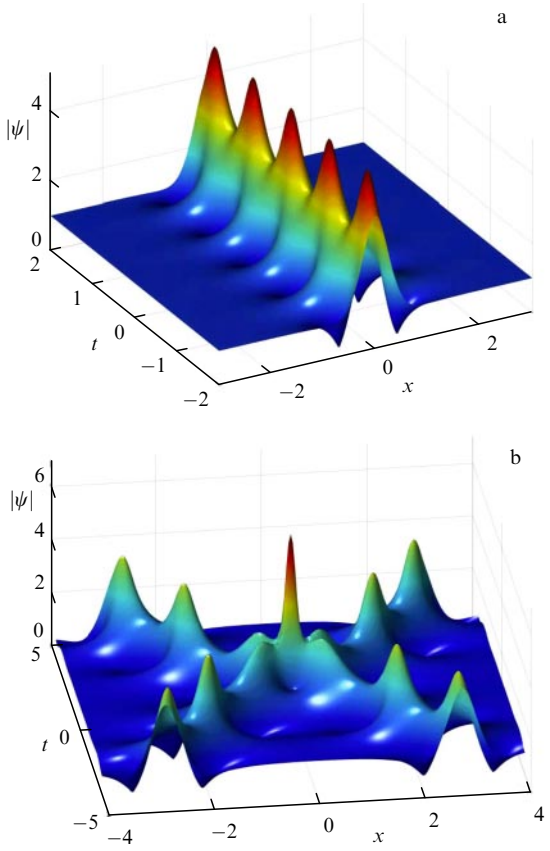

Figure 7. Surface $|\psi(x,t)|$ in space and time coordinates for a Kuznetsov breather with eigenvalue $\zeta = 2$ (a) and for two breathers with eigenvalues $\zeta = 1.5 \pm 0.5\mathrm{i}$ moving toward each other (b).

Floquet theory in the time domain after the spatial domain was reduced to a finite one through the use of periodic boundary conditions. As was shown, the Kuznetsov breather is unstable with the same increment as uniform background waves, but the number of unstable modes depends on the size of the model domain and decreases with a reduction in the spatial period.

Another interesting study concerns the linear instability of Akhmediev breathers in the space of functions periodic in x. Reference [155] argued that solution (45) is linearly unstable if more than one unstable mode fits instability region (43), but it is linearly stable for $L \in (\pi, 2\pi)$ when only one mode fits instability region (43). This assertion is refuted in recent study [156], where the authors constructed explicit solutions of the linearized NSE (51) for $\psi = \psi_{\mathrm{A}}$ given by the Akhmediev solution (45), which grow exponentially with time t in the case of one as well as several unstable modes.

Another way to reach a conclusion about the instability of Akhmediev breathers in the class of periodic functions is through the use of the fourth-order Lax–Novikov equation and variational representation of breathers [157]. A similar approach was applied to the Kuznetsov and Peregrine breathers, which turned out to be energetically unstable in the class of functions decaying into nonzero boundary conditions. Although the breather solutions being discussed are the solution of the third-order Lax–Novikov equation (49), they also satisfy the fourth order equation (and all Lax–Novikov equations of high order), which has been used in Ref. [157].

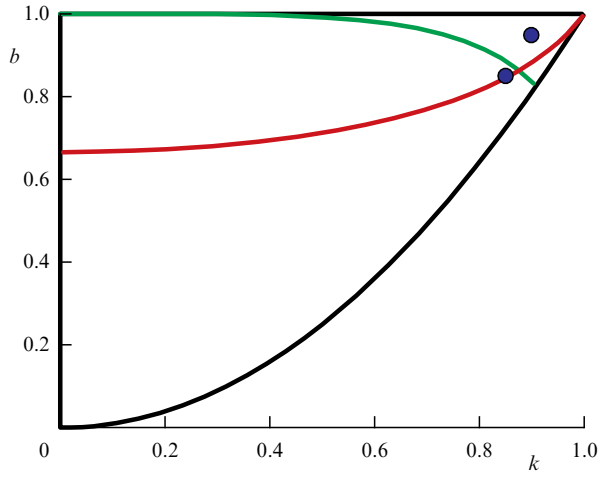

Figure 8. Boundaries of triangular domain on the plane (b,k) where periodic solutions (37) with a nontrivial phase exist.

4.3 Rogue waves on the background of modulated waves

It is known that waves with periodic modulations in the form (32) are unstable to relatively long perturbations [136] (see recent review [158]). In this respect, a natural question arises about the existence of rogue waves on the background of periodically modulated waves, which are analogous to breathers on the background of uniform waves, described above.

Such solutions were first constructed numerically in Ref. [159]. Rogue waves emerging from periodic dnoidal waves (34) were observed in the numerical simulation of time evolution in the framework of the NSE in Ref. [109]. Exact solutions for such rogue waves were elaborated in Ref. [160] and generalized in Ref. [161]. The modulation instability of periodically modulated waves and rogue waves emerging on the background were observed in experiments [162].

The link between the instability of solutions (32) and the occurrence of rogue waves is established in Ref. [137]. The black line in Fig. 8 bounds a domain in the parameter plane b,k, where periodic solutions (37) with a nontrivial phase may exist. The spectra of the Lax system in Fig. 9 are constructed for the set of parameters marked with blue dots in Fig. 8. The black lines in Fig. 9 depict spectral lines, and the red dots correspond to the positions of the roots of the associated polynomial for periodic solutions (37) (see details in Refs [136, 137])

$$P(\zeta) = \zeta^4 - \frac{1}{2}(3b - 1 - k^2)\zeta^2 - \mathrm{i}\sqrt{b(b-k^2)(1-b)}\,\zeta + \frac{1}{16}\left[-3b^2 + 2b(1+k^2) + (1-k^2)^2\right]. \tag{53}$$

Polynomial (53) possesses two symmetric pairs of roots $\{\zeta_{\pm}, -\zeta_{\pm}^{*}\}$,

$$\zeta_{\pm} = \frac{1}{2}\left(\sqrt{b} \pm \sqrt{b-k^2}\right) \pm \frac{\mathrm{i}}{2}\sqrt{1-b}\,. \tag{54}$$

The green curve in Fig. 8 separates two regions with qualitatively different spectra. The spectrum of the scattering problem for periodic solutions in the upper (or lower) domain contains spectral lines intersecting the imaginary (or real) axis in the plane ζ (see Fig. 9).

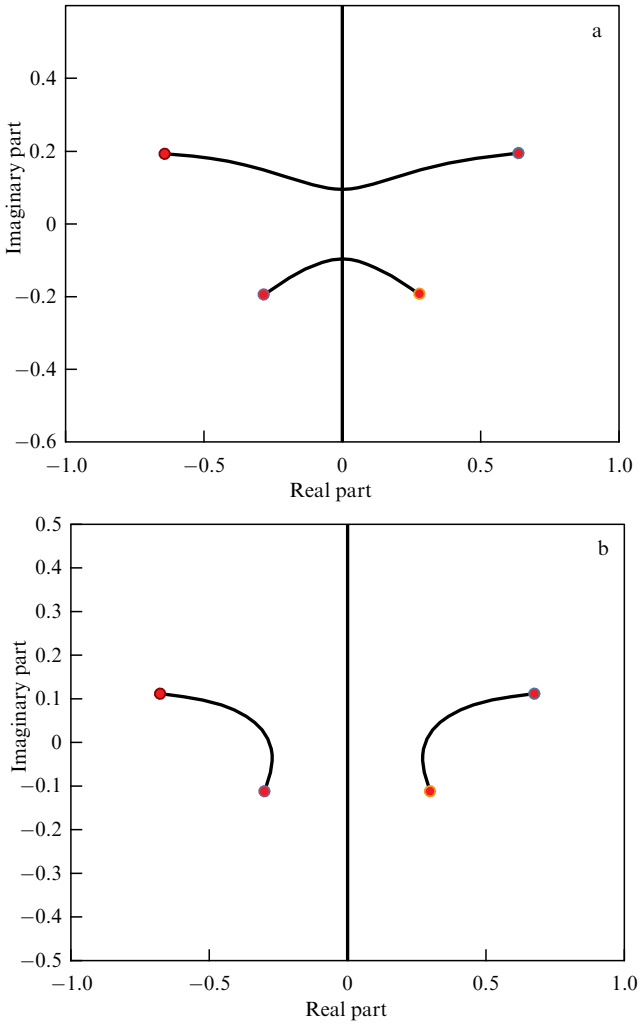

Figure 9. Spectra of the scattering problem on complex plane ζ for periodic solutions (37) with parameters $(b,k)=(0.85,0.85)$ (a) and $(b,k)=(0.95,0.90)$ (b) [137].

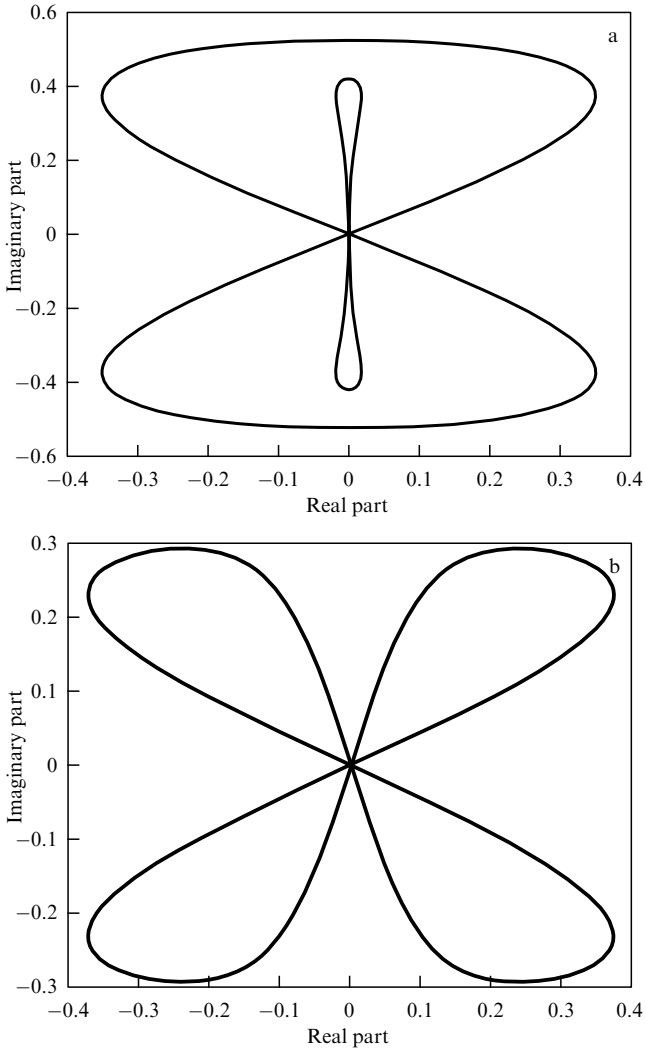

Figure 10. Branches of modulation instability on the complex plane λ for periodic solution (37) with parameters $(b,k)=(0.85,0.85)$ (a) and $(b,k)=(0.95,0.90)$ (b) [137].

The link between the Lax system spectrum and the spectrum of the modulational instability of periodic solutions (32) is explained in Ref. [136]. The substitution with separable variables $\psi(x,t)=u(x)\exp(\mathrm{i}\omega t)$, $v(x,t)=w_1(x)\exp(\mathrm{i}\omega t+\lambda t)$, and $v^*(x,t)=w_2(x)\exp(-\mathrm{i}\omega t+\lambda t)$ reduces the linearized NSE (51) to a problem on the stability of the solution with the spectral parameter λ. This stability problem can be written in the form

$$\mathcal{L}w=\mathrm{i}\lambda\sigma_3 w\,, \tag{55}$$

where $w=(w_1,w_2)^{\mathrm{T}}$, $\sigma_3=\mathrm{diag}\,(1,-1)$, and the linear operator $\mathcal{L}$ takes the form

$$L=\begin{pmatrix} -\dfrac{1}{2}\,\partial_x^2+\omega-2|u|^2 & -u^2 \\ \mathrm{i}u^{*2} & -\dfrac{1}{2}\,\partial_x^2+\omega-2|u|^2 \end{pmatrix}. \tag{56}$$

From the Floquet theory, it follows that the spectrum of problem (55) consists of continuous spectral lines for which the eigenvector w is a bounded quasiperiodic function of coordinate x. Unstable solutions correspond to $\mathrm{Re}\,\lambda>0$. Spectral lines with $\mathrm{Re}\,\lambda>0$ passing through the point $\lambda=0$ correspond to modulation instability of the periodic solution.

The spectrum of problem (55) can be obtained from the spectrum of the Zakharov–Shabat problem (40) with the use of the transformation formula

$$\lambda=\pm 2\mathrm{i}\sqrt{P(\zeta)}\,, \tag{57}$$

where the polynomial $P(\zeta)$ is defined in (53). The stability problem spectrum is plotted in Fig. 10 on the complex plane λ for the same set of parameters as in Fig. 9. Depending on the spectrum of the scattering problem, the stability problem spectrum takes the form of either two eights (Fig. 10a) or a butterfly (Fig. 10b).

Different from the spectrum of modulation instability for plain waves (42), (43), the spectrum λ of unstable perturbations of periodic solutions with a nontrivial phase is no longer real. This property complicates the observation of modulation instability for cnoidal waves (35) or waves with a nontrivial phase (37), reproduced in experiments [162]. Only in the case of dnoidal waves (34), which generalizes the solution for waves of constant amplitude (31), does only one branch of modulation instability located at the real axis exist, analogously to solution (43) [136, 158, 162].

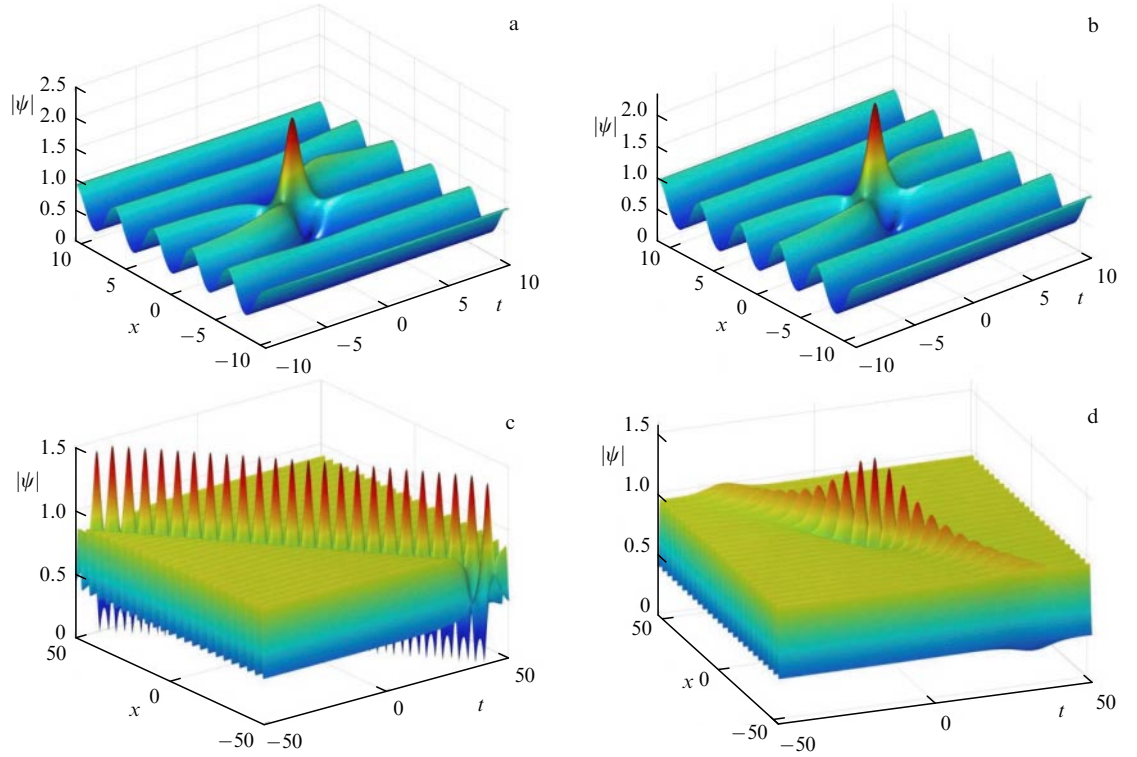

Figure 11. Exact solutions in the form of rogue waves on the background of a periodic wave (37) for parameters $(b, k) = (0.85, 0.85)$ (a, c) and $(b, k) = (0.95, 0.90)$ (b, d). Panels a and b correspond to upper end points of the Lax spectrum in Fig. 9, and panels c and d correspond to lower end points [137].

We explain now the role of the red curve in Fig. 8 and the connection between the modulation instability of periodically modulated waves and the emergence of anomalously high waves in their background. Figures 9a and 10a correspond to a point on the red curve in Fig. 8. The red curve corresponds to the situation when the internal eight on the spectral plane λ is shrinking towards the imaginary axis, as shown in Fig. 10a. This leads to delocalization of anomalously high waves appearing on the periodic background as explained further.

In Ref. [137], solutions in the form of rogue waves were constructed with the help of an algebraic method based on the roots (54) of the polynomial $P(\zeta)$ (53). Figure 11 shows solutions in the form of rogue waves on the background of periodic modulations for the choice of parameters in Figs 9 and 10. The upper row of images corresponds to the root ζ_+, and the lower one corresponds to the root ζ_-.

The wave amplification coefficient defined in (39) was computed in Ref. [137],

$$M_\pm = 2 \pm \sqrt{1 - \frac{k^2}{b}}, \tag{58}$$

where the upper and lower signs correspond to the roots $\zeta_\pm$ in (54). The magnitude of wave amplification is linked to the distance from the root to the imaginary axis in Fig. 9.

For dnoidal waves (34) with $b = 1$, formula (58) gives the dependence $M = 2 \pm (1 - k^2)^{1/2}$, and for cnoidal waves with $b = k^2$, the amplification reaches the value of two, $M = 2$. The amplification coefficient M for these cases was obtained theoretically in Ref. [160] and then confirmed experimentally [162].

Each of the roots $P(\lambda)$ marked by red dots in Fig. 9 is mapped by transform (57) to the coordinate origin point of complex plane λ in Fig. 10. The increment of modulation instability depends on the angle at which the spectral line passes through the point $\lambda = 0$: it is smaller if the line passes closer to the imaginary axis and larger if it is closer to the real axis.

This same angle determines the degree of rogue wave localization. The solution in Fig. 11c corresponds to the internal eight in Fig. 10a contracted along the imaginary axis. This solution is delocalized in the plane (x, t) and in fact presents a soliton propagating on the background of a periodically modulated wave. The solution in Fig. 11d corresponds to that part of the butterfly in Fig. 10b which crosses the coordinate origin closer to the imaginary axis. This solution is localized in the plane (x, t) and corresponds to the definition of a rogue wave (38), although the localization degree is weaker than for rogue waves that correspond to the other branch of the butterfly.

The link between the slope of the modulation instability line in the plane λ for a periodic modulated solution and localization of emerging anomalously high waves was also confirmed by many other examples. For systems of coupled NSEs, Refs [163, 164] drew the conclusion that anomalously high waves on the background of constant amplitude waves can only form in cases unstable to modulation. For subsets of parameters that correspond to modulation stability, constructing rogue-wave solutions was not successful, and large-amplitude localized waves do not arise in direct numerical simulation [165]. Here, it is important to note that, if a solution with a constant amplitude or a periodic solution for the envelope are unstable relative to short perturbations but stable with respect to longer perturbations, the wave is considered to be stable to modulation.

Another example of mathematical rogue waves is given by the sine–Gordon equation [166], where two solutions in the form of periodic waves have different properties of modulation instability [167, 168]. Cnoidal waves are unstable to modulation, and the occurring rogue waves are localized in

space and time. Along with this, dnoidal waves are stable to modulation (but unstable with respect to perturbations with a smaller spatial scale) and solutions in the form of rogue waves degenerate in propagating solitons. A similar situation is observed in the framework of the modified Korteweg–de Vries equation [169].

4.4 More complex structures of rogue waves

More complex quasi-periodic wave patterns are described by exact solutions of the NSE (30) in terms of Riemann theta function [170–173]. The Riemann theta function describes a general solution of the third-order Lax–Novikov equation (49) and in special cases is reduced to rational functions of the Jacobi elliptic functions, as found in Ref. [34]. In the latter case, the solutions are periodic in both time and space. It can be guessed that these doubly-periodic solutions describe an intermediate stage preceding the onset of chaotic waves as the result of developing modulational instability of plane waves.

Two families of doubly-periodic solutions describe background waves [174]: with the repeating phases of modulations (Fig. 12a) and with alternating phases (Fig. 12b). The Lax system spectra that correspond to them are plotted in Fig. 6a and 6b. These two families generalize solutions in the form of Akhmediev breathers (45), which can be explicitly seen from the spectra, as described in Section 4.2. Experimental observations of doubly periodic solutions as perturbations of Akhmediev breathers were mentioned in Refs [175, 176].

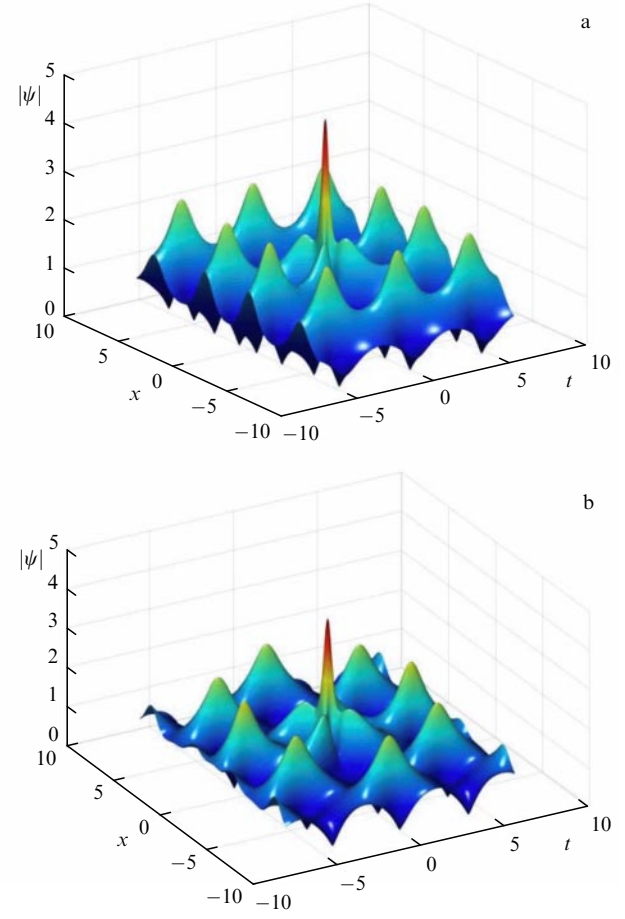

Figure 12. Solutions in the form of rogue waves appearing on the background of doubly periodic solutions. Solutions correspond to the Lax system spectrum plotted in Fig. 6: to the eigenvalue $\sqrt{z_3}$ (a) and $\sqrt{z_1}$ (b) [144].

Solutions describing the emergence of rogue waves on the background of doubly-periodic solutions are constructed analytically and numerically in Ref. [144]. The growth rates of doubly-periodic solutions are computed in Ref. [158] based on a numerical analysis of Lax system equations and also obtained through the results of direct numerical simulation of the NSE in Ref. [177]. Reference [158] shows that the increment of modulations is larger for a uniform wave than for a doubly-periodic solution with an equivalent amplitude. Just as in the cases described above, anomalously high waves emerging on the background of doubly-periodic solutions for the envelope are attributed to the instability of the background wave.

Figure 12 presents solutions describing rogue waves on the background of periodically modulated waves. For each eigenvalue of the Lax system spectrum located at the ends of spectral lines in Fig. 6, a solution can be constructed in the form of a rogue wave localized in space and time. In this case, the wave amplification coefficient is maximal for the eigenvalue which is furthest from the imaginary axis. Namely solutions characterized by maximum amplification are shown in Fig. 12.

5. Direct modeling of sea waves

5.1 Conventional approach

The description of sea waves in prognostic models (WAM, WaveWatch, SWAN) is based on the spectral kinetic theory (the Hasselmann equations). The balance equations for the spectral density of wave action $N(\mathbf{k},\mathbf{x},t)=E(\mathbf{k},\mathbf{x},t)/\omega(\mathbf{k})$, where E is the surface density of the total mechanical energy, are written in a conservative form as [71, 72, 96]

$$\frac{\partial N}{\partial t}+\nabla_{\mathbf{x}}(\mathbf{c}_{\mathrm{gr}}N)=S_{\mathrm{nl}}\,,\quad \mathbf{c}_{\mathrm{gr}}=\nabla_{\mathbf{k}}\omega\,, \tag{59}$$

$$\begin{aligned} S_{\mathrm{nl}} = 4\int\int\int |T_{\mathbf{kk_1k_2k_3}}|^2 (N_1N_2N_3 + NN_2N_3 - NN_1N_2 \\ - NN_1N_3)\,\mathrm{Im}\left[G(\Delta\omega,t)\right]\delta(\mathbf{k}+\mathbf{k}_1-\mathbf{k}_2-\mathbf{k}_3) \\ \times\ \mathrm{d}\mathbf{k}_1\,\mathrm{d}\mathbf{k}_2\,\mathrm{d}\mathbf{k}_3\,, \end{aligned} \tag{60}$$

$$\Delta\omega=\omega+\omega_1-\omega_2-\omega_3\,,$$

$$G(\Delta\omega,t)=\frac{1-\exp\left(-\mathrm{i}\Delta\omega t\right)}{\Delta\omega}\,,$$

where the relationship between the wave vectors and frequencies is given by the linear dispersion relation. Expression (60) for the collision integral S_{nl}, which is obtained from the spectral Zakharov equations (16) under the assumption of weak deviation from the Gaussian process, contains the coefficient of 4-wave interactions $T_{\mathbf{kk_1k_2k_3}}$. The derivation of system (59), (60) relies on the independence of random wave phases (a closure hypothesis). A nonconservative form of kinetic equation (59) takes into account the effects of wind and dissipation, but there is no rigorous derivation for their form from first principles.

In the 'classical' variant of the kinetic equation, the limit of large time is used under the assumption that the wave action varies slowly, in which case $\mathrm{Im}\,G(\Delta\omega,t)\to\pi\delta(\Delta\omega)$ and the evolution is only affected by resonant nonlinear interactions which nullify the function of difference frequency $\Delta\omega$, which simplifies computations of integral S_{nl}. For homogeneous

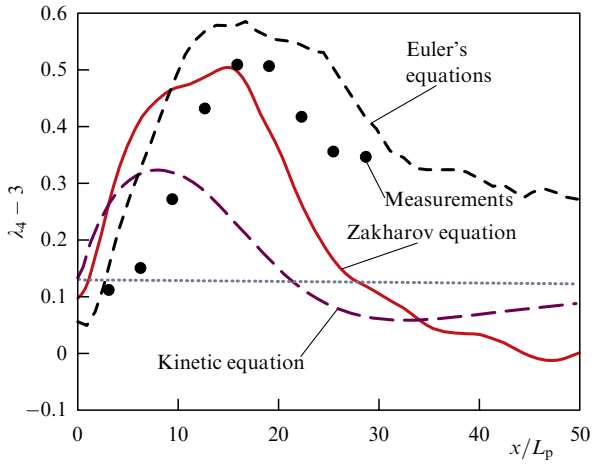

Figure 13. Evolution of surface displacement excess kurtosis $\lambda_4 - 3$ based on the results of numerical modeling of the modified kinetic equation, the Zakharov equation, the HOSM code for Euler's equations, and laboratory measurements. Abscissa corresponds to the distance normalized by the wavelength of waves that correspond to the spectral peak [179].

conditions, the characteristic evolution time scale follows from equation (60): for the 'classical' case this is the so-called *kinetic* scale $O(\omega_0\varepsilon^{-4})$, where ω_0 is the characteristic frequency, and $\varepsilon = k_0\sigma$ is the nonlinearity parameter. At small times $\mathrm{Im}\, G(\Delta\omega, t) \approx t$, and then a faster scale, the so-called *dynamic* scale, $O(\omega_0\varepsilon^{-2})$ is present. A fast evolution of wave spectra was observed through direct numerical simulation of the Zakharov equations in Refs [116, 117]. As shown below, modulation instability and the related increased probability of observing rogue waves develop on a dynamic time scale. To account for fast wave interactions, Refs [83, 113, 178] proposed versions of the kinetic equation that take into account the dependence of function G on time.

An example of the evolution of the fourth statistical moment for the same conditions comprising irregular waves with a narrowband initial spectrum is presented in Fig. 13 [179] based on computations with the kinetic equation which took into account the time dependence of function G, computations based on the phase-resolving Zakharov equations, and computations based on the solution of hydrodynamic equations in the original formulation. As can be seen from the figure, even though there is approximate similarity in the behavior of the curves, they demonstrate a noticeable difference. Computations based on the primitive equations of hydrodynamics reproduce the laboratory measurements (shown by dots) better than the others do.

To model the effects of strong nonlinearity and coherent and rapidly evolving processes, one needs computations of dynamical equations which resolve the wave phases. The tasks of forecasts and computations of statistical distributions require 'fast' evolution models and numerical codes. Further, a brief review of such models is given, with particular attention paid to the case of deep water; the results of their use for exploring rogue waves are presented, in comparison to the data from laboratory and field experiments.

5.2 Fast models for the description of surface wave dynamics

Under the assumption of a narrowband spectrum with a dominant wavenumber k_0 and frequency $\omega_0 = \omega(k_0)$, the Zakharov equations lead to the NSE for the complex envelope $A(x, t)$ [26, 69],

$$-\mathrm{i}\left(\frac{\partial A}{\partial t} + c_{\mathrm{gr}}\frac{\partial A}{\partial x}\right) + \alpha|A|^2 + \beta\frac{\partial^2 A}{\partial x^2} = 0\,, \tag{61}$$

$$\eta(x, t) = \mathrm{Re}\left[A(x, t)\exp\left(\mathrm{i}k_0 x - \mathrm{i}\omega_0 t\right)\right], \tag{62}$$

which is fully integrable with the help of IST (see Section 4). Equation (61) can be reduced to the dimensionless form (30) for the function $\psi(x', t')$ after the transformations

$$x' = \sqrt{\frac{\omega_0}{4\beta}}\,(x - c_{\mathrm{gr}}t)\,, \quad t' = \frac{\omega_0}{2}\,t\,, \quad \psi = \sqrt{\frac{2\alpha}{\omega_0}}\,A^*\,. \tag{63}$$

The NSE takes into account effects of the third order $O(\varepsilon^3)$ of weak nonlinearity and dispersion, $\delta_k = O(\varepsilon)$. The real coefficients of equation (61) are the functions of dimensionless depth k_0h, and $\beta > 0$. The nonlinear coefficient α changes sign at $k_0h = 1.363$ and for large depths ensures the fulfillment of the criterion that the medium be unstable to modulation, $\alpha\beta > 0$.

Asymptotic models of modulated waves of higher order have been presented in the literature (see, for example, Refs [180, 181]), but the most popular ones are modifications of the Dysthe equation [182, 183], which is a nonlocal generalization of the NSE of fourth order, $O(\varepsilon^4)$, for sufficiently deep water, $k_0h \geqslant O(\varepsilon^{-1})$. The evolution equation describes the wave amplitude $A(x, t)$, where the potential of the induced flow $\bar{\varphi}(x, z, t)$ is found from Laplace's equation with given boundary conditions at the bottom and unperturbed surface $z = 0$,

$$-\mathrm{i}\frac{\partial A}{\partial t} + \hat{L}\left[\frac{\partial}{\partial x}\right]A + \frac{\omega_0 k_0^2}{2}|A|^2 A - \mathrm{i}\,\frac{3\omega_0 k_0}{2}|A|^2\frac{\partial A}{\partial x}$$

$$-\mathrm{i}\,\frac{\omega_0 k_0}{4}\,A^2\frac{\partial A^*}{\partial x} + k_0 A\,\frac{\partial\bar{\varphi}|_{z=0}}{\partial x} = 0\,, \tag{64}$$

$$\frac{\partial^2\bar{\varphi}}{\partial x^2} + \frac{\partial^2\bar{\varphi}}{\partial z^2} = 0\,, \qquad -h \leqslant z \leqslant \eta;$$

$$\frac{\partial\bar{\varphi}}{\partial z} = \frac{\omega_0}{2}\,\frac{\partial}{\partial x}\,|A|^2\,, \qquad z = 0; \qquad \frac{\partial\bar{\varphi}}{\partial z} = 0\,, \quad z = -h\,.$$

In the first approximation, the surface displacement $\eta(x, t)$ is computed from formula (62) (formulas of reconstruction with $O(\varepsilon^3)$ accuracy can be found in Ref. [184]). The dispersion operator, which has the form $\hat{L}_k = \sqrt{g(k_0 + k)} - \omega_0$ in the Fourier representation, describes a linear solution of hydrodynamical equations. The classical NSE (61) in the limit of deep water follows from (64) by omitting the last three terms in the evolution equation and reducing dispersion to $\hat{L}A = \omega_0 A_{xx}/(8k_0^2) + O(\varepsilon^4)$. For brevity, we present here versions of the equation for the envelope (61), (64) without accounting for the transverse surface coordinate.

In plane geometry (one horizontal coordinate), equations of hydrodynamics can be efficiently solved by conformal mapping, which reduces the domain $Z = x + \mathrm{i}z$ filled with fluid, bounded at the top by a nonstationary free surface $z = \eta(x, t)$, to the layer $W = u + \mathrm{i}v$ with a constant upper boundary $v = 0$. In the case of infinitely deep water, such a transform is written as

$$z = \hat{H}\left\{x(u, t) - u\right\}, \quad x(u, t) = u - \hat{H}\left\{z(u, t)\right\}, \tag{65}$$

where $\hat{H}$ is the Hilbert transform operator. In this case, the full system of hydrodynamical equations (5)–(8) can be reduced to equations with cubic nonlinearity in conformal variables [185, 186],

$$R_t = \mathrm{i}(UR_W - RU_W)\,, \quad V_t = \mathrm{i}(UV_W - RB_W) + g(R-1)\,, \tag{66}$$

$$U = \hat{P}\{VR^* + V^*R\}\,, \quad B = \hat{P}\{VV^*\}\,, \quad \hat{P} = \frac{1}{2}(1 + \mathrm{i}\hat{H})\,,$$

$$R = \frac{1}{Z_W}\,, \quad V = \mathrm{i}\,\frac{1}{Z_W}\,\frac{\partial}{\partial W}\left(\Phi + \mathrm{i}\hat{H}\{\Phi\}\right). \tag{67}$$

Here, Φ is the velocity potential on the surface, as earlier. A numerical set of equations for $R(W,t)$ and $V(W,t)$ (66) (Dyachenko–Zakharov equations) demonstrates high speed and stability. Reference [187] shows an exclusively high computational accuracy in computations of the evolution of very steep waves for 1000 periods using equations formulated in conformal variables $Z(W,t)$ and $\Phi(W,t)$. There are generalizations of the model in conformal variables in the literature for the cases of finite depth, a time-varying bottom, and quasiplanar waves [188, 189]. Recent studies [190, 191] propose new analytical approaches based on conformal mapping for a more efficient description of very steep waves.

A pseudospectral method of high nonlinear order (High Order Spectral Method, HOSM) proposed independently in Refs [192, 193] to solve the full potential equations of hydrodynamics (5)–(8) shows a faster performance than the Zakharov equations with the analogous nonlinearity order. In the HOSM, to compute the vertical velocity components that enter (7), (8), an exact solution of Laplace's equation (5) is used at each time step in the fixed domain bounded from the top by the unperturbed surface level $z = 0$. The velocity potential $\varphi(\mathbf{x}, z, t)$ is presented as an asymptotic series $\varphi^{(m)}$ in small wave steepness parameter ε, and the transfer of the surface potential $\Phi(\mathbf{x}, t)$ to the level $z = 0$ is carried out with the help of the inversion of the expansion of the potential in Taylor series $\varphi(\mathbf{x}, z, t)$ around $z = 0$ up to an arbitrary order M,

$$\varphi = \sum_{m=1}^{M} \varphi^{(m)}(\mathbf{x}, z, t)\,,$$

$$\Phi(\mathbf{x}, t) = \sum_{m=1}^{M} \sum_{n=0}^{M-m} \frac{\eta^n}{n!}\,\frac{\partial^n}{\partial z^n}\,\varphi^{(m)}(\mathbf{x}, z=0, t)\,, \tag{68}$$

$$\varphi^{(m)} = \sum_{n=0}^{\infty} \varphi_n^{(m)}(t)\,\frac{\cosh\left(|\mathbf{k}_n|(z+h)\right)}{\cosh\left(|\mathbf{k}_n|h\right)}\,\exp\left(\mathrm{i}\mathbf{k}_n\mathbf{x}\right).$$

The parameter M governs the degree of model nonlinearity. The HOSM scheme in formulation of Ref. [193] is equivalent to the 4-wave Hamiltonian Zakharov equations for the choice $M = 3$ [194]. References [195, 196] proposed HOSM modifications to describe waves on inhomogeneous bathymetry and currents, and improved the convergence of the method as applied to very steep waves.

Because of the limited capability of the HOSM to describe steep waves of different lengths (see [37, 38]), Ref. [197] proposed a new fast method to solve equations (5)–(8) with a high accuracy in an accompanying curvilinear reference frame, which employs an analytical solution of Laplace's equation as the first approximation.

We mention a set of new models, all being a modification of the Zakharov equations for the case of unidirectional waves, so-called compact and super-compact equations [189–200]. Their derivation is based on a new canonical transform from $b_k(t)$ (see (16)) to variables $c_k(t)$ and a set of simplifications based on symmetry properties of four-wave interaction coefficient $T_{\mathbf{kk_1k_2k_3}}$ and its approximation on resonance surfaces. The compact equations take a simple form in both spectral and physical spaces and also allow the so-called spatial formulation when the coordinate becomes the evolution variable instead of time. It is essential that the supercompact equation have an exact solution in the form of a soliton-like short group of steep waves [199]; the equation does not have a formal limitation on the spectral width (see Section 5.5).

5.3 Stochastic numerical simulation of sea waves

A special role in the solution to the rogue wave problem is played by direct phase-resolving numerical modeling of irregular waves, which allows one to connect spectral characteristics (which are the output data of the existing prognostic sea wave model) and wave probability properties under minimum assumptions. Most frequently, a problem statement is used that for a wave spectrum given at the initial time moment $t = 0$ the wave evolution is computed for some time interval $0 < t < T$. Subsequent statistical processing is carried out for an ensemble of realizations of initial conditions with random phases, and sometimes also with averaging over the time period T. For not very large simulation interval T, one commonly ignores the effects of wind forcing and wave decay. A dominant part of stochastic numerical simulation is carried out in the framework of models listed in Section 5.2. A set of laboratory experiments appears to be analogous, with the difference being that, instead of an initial condition, the wavemaker creates a boundary condition on one basin side, and wave evolution is studied as waves propagate along the basin.

Spectra of model forms are commonly used in computations, including the JONSWAP spectrum based on the results of long-term measurements in the North Sea [96],

$$S(\omega) = \frac{\alpha_{\mathrm{P}} g^2}{\omega^5}\,\exp\left[-\frac{5}{4}\,\frac{\omega_{\mathrm{p}}^4}{\omega^4}\right]\gamma^{\exp\left[-\frac{1}{2}\,\frac{(\omega-\omega_{\mathrm{p}})^2}{\sigma^2\omega_{\mathrm{p}}^2}\right]}. \tag{69}$$

Here, ω_{p} is the spectral peak frequency, α_{P} is the Phillips parameter which governs wave intensity, and the parameter $\sigma = 0.07$ and $\sigma = 0.09$ for $\omega \leqslant \omega_{\mathrm{p}}$ and $\omega \geqslant \omega_{\mathrm{p}}$, respectively. For the peak enhancement factor γ equal to one, expression (69) coincides in form with the classical Pierson–Moskowitz spectrum [23]. For large values of the peakedness factor, the spectrum becomes in effect narrower.

A fundamental difficulty in modeling large waves consists in accounting for wave breaking [201]. Solutions of primitive equations (5)–(8) should be single-valued functions of coordinates. In conformal variables, the surface is described parametrically and can be a multivalued function of the horizontal coordinate, but without self-crossings. If there are large slopes (even at a single spatial point), the Fourier series begins to converge slowly, which leads to instability of short waves in the framework of spectral numerical codes. Since fast models are required for statistical modeling, the effects of breaking are parameterized with the use of spectral filters or the addition of artificial dissipation in the region of short

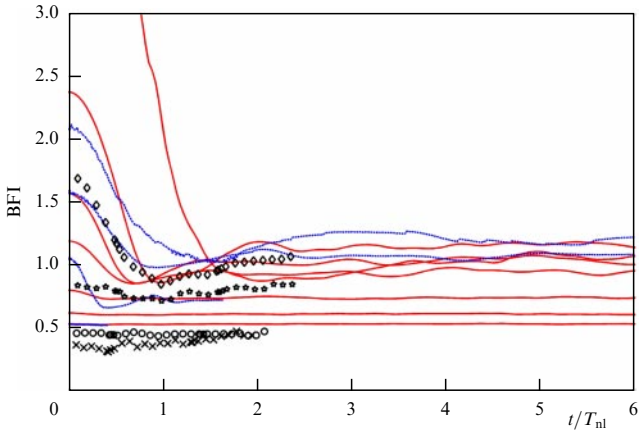

Figure 14. Evolution of instantaneous BFI using data of numerical simulation of unidirectional waves in the framework of the NSE (red solid lines), full Euler's equations (blue dotted lines), and laboratory measurements (symbols) [209].

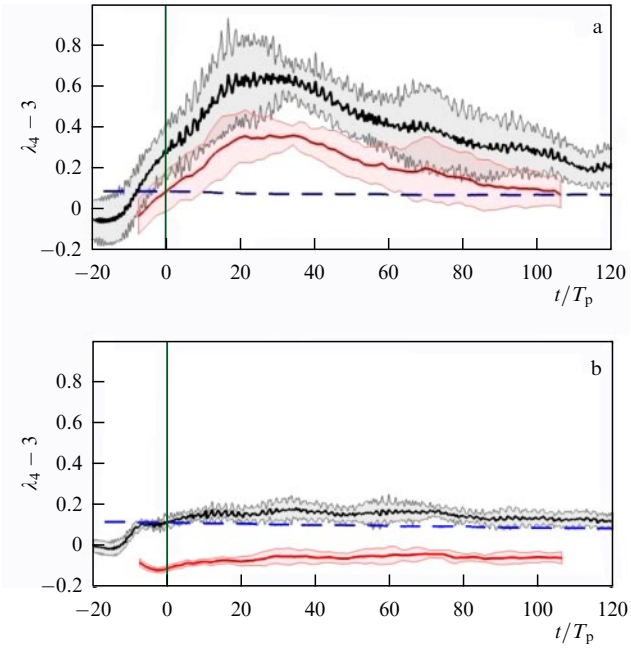

Figure 15. Evolution of full $\lambda_4 - 3$ (black curves) and dynamic $\lambda_4^{\rm dyn}$ (red curves) surface displacement excess kurtosis based on numerical simulation of Euler's equations by the HOSM ($M = 3$) for conditions $T_{\rm p} = 10$ s, $H_{\rm s} = 6-7$ m, and half-width of the directional spectrum of 6° (a) and 30° (b). Horizontal dashed line is the estimate of the excess kurtosis of bound waves $\lambda_4^{\rm bound}$ (24). Time interval $t < 0$ corresponds to the preparatory stage when computations were initialized [210].

waves [94, 197, 203]. Sometimes, to compensate for energy losses, forcing is added [203, 204]. Another strategy consists in computations without parameterized wave breaking up to the moment the first wave breaks (not necessarily the highest one), when the numerical scheme is brought to a halt because of numerical instability [205, 206]. All the approaches listed here have their own drawbacks and can lead to systematic errors in the description of wave height probabilities.

In a large number of numerical and laboratory experiments (e.g., [92,114, 115, 179, 207, 208]), it is demonstrated that, if, for a fixed intensity, the spectrum of initial conditions is sufficiently narrowband, then its fast broadening takes place, accompanied by the growth of excess kurtosis (see Fig. 13) and an increased probability of high waves. Unstable states are identified well by the index of modulation instability BFI (23). Figure 14 plots the graphs of the dynamics of instantaneous BFI values based on computations of unidirectional waves with a Gaussian spectrum in the framework of the NSE and Dyachenko–Zakharov conformal equations, and also on data from field measurements in a 300-m hydrodynamical basin [207, 209]. Initial conditions from the region BFI < 1 prove to be stable and at the times considered do not demonstrate noticeable changes in wave statistics. For BFI > 1, the system returns to a stable state through a characteristic time which corresponds to the dynamical scale $T_{\rm nl} = \omega_0^{-1}\varepsilon^{-2}$. During this time interval, the probability that a very high wave may occur increases, which is reflected in a short-term increase in the excess kurtosis of surface displacement, as shown in Fig. 15a.

A substantial growth in surface displacement excess kurtosis on the dynamic scale time, coming from its dynamic part of kurtosis $\lambda^{\rm dyn}$ after a sudden wind change, is demonstrated in the numerical modeling of the Zakharov equations [116]. In Ref. [210], where the dynamic part of kurtosis was retrieved from the data of direct numerical simulation of Euler's equations, it is shown that the role of dynamic kurtosis is important in nonequilibrium situations with intense waves, which have a relatively narrow angular spectrum, as is seen from Fig. 15a. In the opposite case of a wide spectrum, the main contribution in excess kurtosis (and the related deviation from the Gaussian statistics) is made by bound waves (Fig. 15b). Under such conditions, statistical moments are defined by the shape of the spectrum (phase relationships between waves are not important), and, using numerical methods to compute the six-dimensional integral (21), they can be presented as parameterized realistic spectra (such as JONSWAP) [211], which gives a practical instrument for probabilistic wave description in stationary conditions.

The probability distributions for wave heights computed through numerical simulation of unidirectional waves with the JONSWAP spectrum for $\gamma = 3$ and moderate nonlinearity $k_{\rm p}\sigma \approx 0.035$ (there is practically no breaking) in the HOSM framework ($M = 6$) are given in Fig. 16. They agree with the Rayleigh distribution in the interval of waves with relatively small heights and demonstrate a significant difference for high waves, $H > 2H_{1/3}$.

It is plausible to assume that the majority of sea wave spectra correspond to equilibrium conditions of a sufficiently wide spectrum. In particular, in Ref. [212], based on the modeling of the generalization of the Alber equation for a broadband spectrum, a conclusion is drawn on the stability of sea wave states with $\gamma \leqslant 1$ for arbitrary realistic wave heights. This circumstance could help explain the paradox that, on averaging over large ensembles of field measurements, the deviation in wave height probability distribution from the Rayleigh distribution turns out to be unnoticeable [52, 213, 214]. To assess the danger of rogue waves and the feasibility of forecasting them, one needs to explore the mechanisms leading to the occurrence of nonequilibrium conditions on the sea, in particular, spectra with narrow intense peaks.

5.4 Characteristic portrait of a rogue wave

Because of dispersion, which is strongest for large depths, wave groups move more slowly than individual waves. The largest surface displacement in groups is observed at those

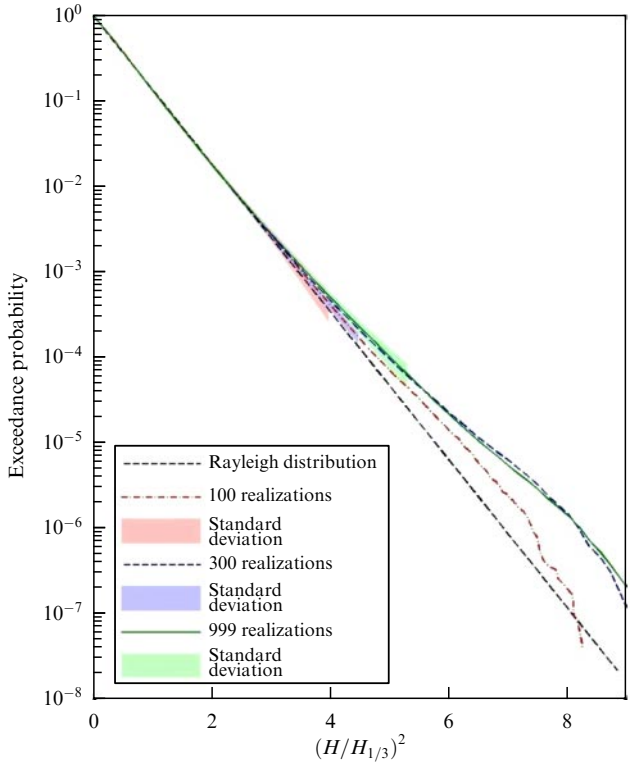

Figure 16. Height probability distribution for unidirectional waves based on numerical modeling results (JONSWAP spectrum), $T_p = 10$ s, $H_s = 3.5$ m, $\gamma = 3$) in comparison with the Rayleigh distribution (2). Three lines correspond to ensembles of 100, 300, and 999 random realizations; color shading is an estimate of significance range [250].

time moments when the wave peak coincides with the maximum of the group envelope. Because of nonlinear corrections, the height of crests is larger than the depths of troughs. From this simple reasoning, it follows that rogue waves should be expected in the form of very high crests surrounded by lower amplitude waves. Computed configurations of wave trains containing anomalous waves can be obtained in the framework of linear theory (the so-called *New Wave theory*) or its weakly nonlinear generalization (see Refs [65, 215, 216]) or by direct numerical simulation of hydrodynamical equations [90, 94, 217–225].

Indeed, for extreme waves characterized by higher sharp crests, such profiles are dominant among computed waves with AI > 2. Waves of large amplitude that evolve as the result of modulation instability acquire much higher energy in the process of focusing than their neighboring waves; with the growth in wave steepness, the concentration of wave energy increases even more [218, 220]. These waves are close in shape to the examples of field measurements in Figs 1 and 5. However, waves of other forms, given in Figs 3 and 4, form too [219]. Based on the result of numerical simulation, it was pointed out that the dominant part of rogue waves has a steeper rear slope (the trough behind the wave is deeper than ahead) [94, 219, 224, 225] (Fig. 17), which agrees with field measurements in Ref. [58]. Such an asymmetry is manifested only under conditions of intense waves and becomes stronger with the broadening of the angular spectrum [225], which does not conform with the mechanism of modulation instability and still calls for an explanation.

Scanties is the view on the volume portrait which is obtained in three-dimensional numerical simulations [94,

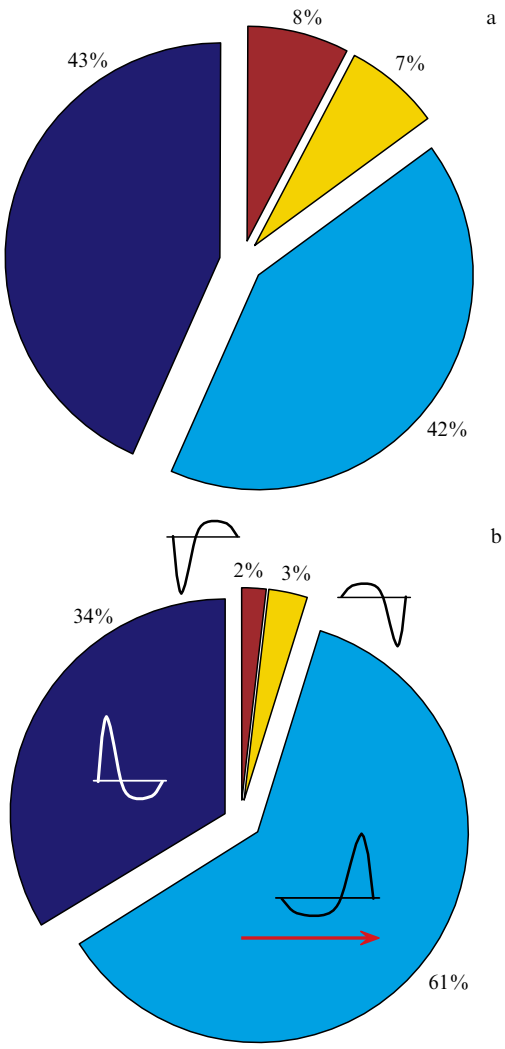

Figure 17. Characteristic distribution of wave forms with AI > 2 via data from direct numerical simulation of irregular waves with moderate (a) and strong (b) nonlinearity [225]. Arrow shows the wave propagation direction.

333]. References [217, 226] mention that anomalously high waves typically appear at zigzag-type patterns of surface waves which propagate at the optimum angle to the wave fronts. A more diverse picture of rogue waves in wave fields with a broadband spectrum was observed in Ref. [227].

Eyewitnesses usually mention the transience of rogue wave events, which can also be a consequence of large wave propagation speeds (during one period, 10-second waves cover about 80 m on deep water). By following the evolution of an intense wave in numerical experiments, characteristic 'lifetimes' of rogue waves were estimated. On the whole, larger wave amplification is observed in lengthier events, as shown in Fig. 18; the unexpectedly large duration of extreme events can be pointed out. References [225, 227, 228] construct probability distributions for the time span of rogue waves. If the width of the angular spectrum is not too large, waves in the intense wave background may exceed the threshold AI $= 2$ during several ten periods. Rogue waves live substantially less time in conditions of a wide angular spectrum and weak nonlinearity, even in comparison with a linear solution.

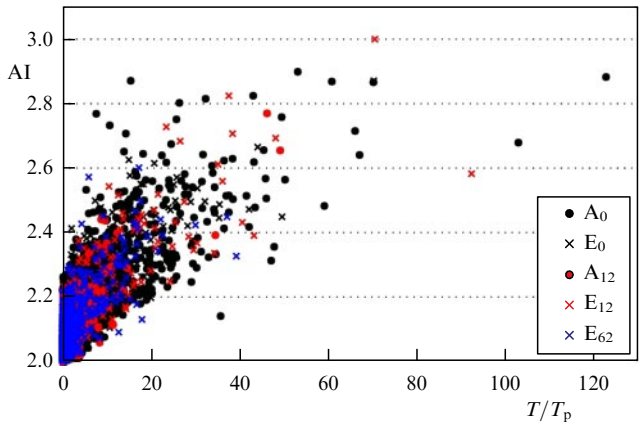

Figure 18. Amplification coefficient AI as a function of the duration of extreme events AI > 2 in wave periods $T_p = 10$ s from data of direct numerical modeling [227]. Cases A and E are related to moderate ($H_s = 3.5$ m) and strong ($H_s = 6-7$ m) nonlinearity, respectively. Subscripts give characteristic width of angular spectrum in degrees.

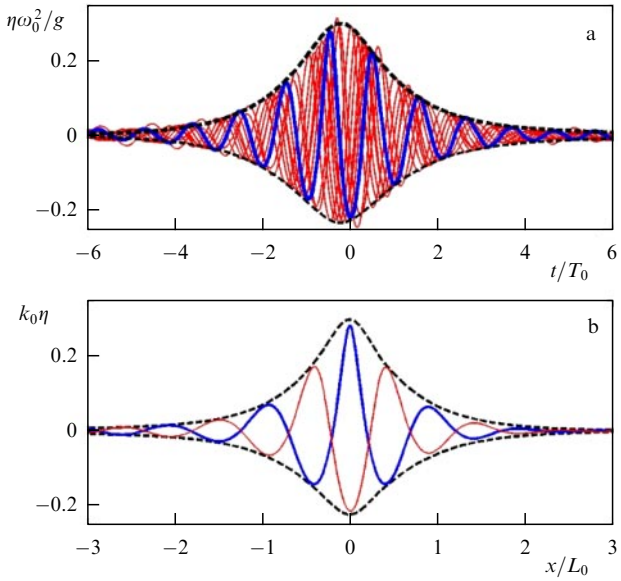

Figure 19. Stationary wave group with maximum steepness on deep water using results of laboratory experiments [231]. (a) Surface displacement records at different gauges (solid lines) and an envelope based on Euler's equations modeling (dashed line). (b) Two instantaneous profiles and an effective envelope from numerical simulation results.

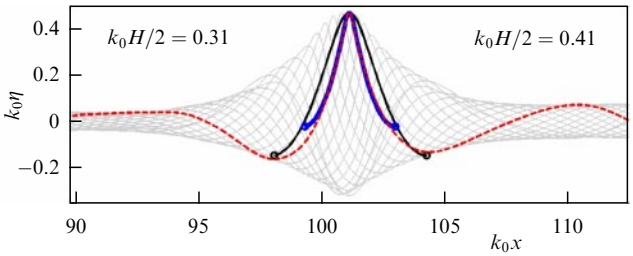

Figure 20. Example of a nonbreaking wave with maximum amplitude amplification based on numerical simulation of unstable unidirectional waves [240]. Red dashed curve gives an instantaneous profile of a wave with maximum displacement, gray curves correspond to profiles in adjacent time moments in a co-moving coordinate system. Thin black and thick blue curves show profiles of uniform Stokes waves fit to local extrema (steepness estimate is given in the left part of the plot) and the crest (steepness estimate is in the right part of the plot) of a maximal wave.

5.5 Strongly nonlinear solitons and breathers on the water surface

Soliton-like wave groups with a steepness approaching the breaking threshold were discovered in Ref. [229] in the framework of a numerical solution of hydrodynamical equations on deep water in conformal variables. Because of strong shape variability (the group contained a couple of waves propagating twice as fast as the group proper), such solutions are sometimes referred to as breathers. Reference [230] showed that such groups are satisfactorily described in the framework of the weakly nonlinear theory of modulated waves (64) for values of steepness up to $k_0|A| \approx 0.2$, where $|A|$ is the maximum amplitude and k_0 is the characteristic wave number.

The discovered 'limiting' envelope solitons were reproduced in laboratory experiments [231, 232], and it has been shown that a soliton solution of the standard NSE (36) can be used for their generation. Instrumental records of the most intense and shortest laboratory envelope soliton are displayed in Fig. 19a (time sequences). The respective instantaneous profiles are plotted in Fig. 19b from the results of direct numerical computations. The steepness of the envelope soliton in Fig. 19 is estimated as $k_0|A| \approx 0.3$ by maximum surface displacement or as $k_0H/2 \approx 0.25$ by wave height. Thus, structurally stable solitary nonlinear trains of collinear waves on a deep water surface exist in practically the entire range of wave steepness — up to reaching the local breaking threshold. In laboratory experiments [232], it is shown that intense soliton groups can interact in almost an elastic way, similar to envelope solitons of the integrable NSE. Propagation and numerous interactions of intense envelope solitons in numerical simulations based on compact and full equations were also explored and compared with the results of integrable theory in Refs [199, 233–235].

The NSE breathers, proposed as prototypes of rogue waves, including solutions of a higher order, were modeled in the framework of full hydrodynamical equations and in laboratory conditions [236–241] (see also Section 4). As a general conclusion, one can say that weakly nonlinear breather solutions of the NSE are reproduced with satisfactory accuracy at certain finite time intervals and demonstrate the emergence of a large-amplitude wave 'out of nowhere' with subsequent (incomplete) demodulation. When several unstable modes compete, the wave evolution at large times can strongly differ from the analytical solution. The forms of rogue waves which correspond to maximum amplification of modulationally unstable wave packets up to the threshold of breaking were explored in Ref. [240]. The emerging extreme waves turned out to be very similar in shape for various seed conditions [239], with narrower crests than in uniform Stokes waves (Fig. 20).

Wave groups in fields of random waves, similar to envelope solitons and Peregrine breathers, and their link to extreme events have been mentioned in many publications (see, for example, Refs [238, 242–249]). Recent paper [250] performed an analysis of the evolution of irregular waves through numerical simulations of Euler's equations, where the formation of a long-lived group of soliton-like intense waves was observed. Despite the strong nonlinearity of the solution and a broadband wave spectrum, the parameters of the soliton (speed and amplitude) varied weakly during more than 200 periods. The majority of high-amplitude waves appeared on its background.

5.6 Reconstruction of sea rogue waves

Direct numerical simulations is used to reconstruct anomalously high waves based on displacement measurement data at a point and also to reproduce the state of the sea when such waves were observed. In the first case, the problem consists in finding hydrodynamical fields near the observation place. Given a temporal series of surface displacement $\eta(x = x_0, t)$, one can recover the surface potential $\Phi(x_0, t)$ under the assumption of unidirectional waves in the framework of approximate nonlinear dispersive models. To compute the wave evolution along, $x > x_0$, and against, $x < x_0$, the spatial versions of asymptotic equations are used [184, 251]. The fidelity of the resulting reconstruction of instrumentally measured sea rogue waves was confirmed in Ref. [184] through juxtaposition with the results obtained by integration of full hydrodynamical equations.

The fundamental importance of taking into account three-dimensional dynamics in the formation of the New Year Wave (see Fig. 1) was asserted in Ref. [252] on the basis of mean upward displacement of the group containing the New Year Wave, which is not typical of the NSE theory. A qualitative difference in time records of extreme waves which arise in collisions of co- and oppositely moving envelope solitons was mentioned in Ref. [232]. Thus, using the results of nonlinear theory, the dynamics of anomalous waves can be recovered based on indirect evidence.

Reconstructions of measured rogue waves were also carried out in laboratory tanks with the use of weakly nonlinear theory to compute the boundary condition of a wavemaker, with subsequent refinement in an iterative procedure. For example, the New Year Wave was re-created in the field of unidirectional waves [253] and under the assumption of a bi-modal character — as the result of waves propagating at an angle to each other [254].

In the framework of the second direction, dangerous sea states were reconstructed by direct numerical simulations of hydrodynamical equations with initial conditions in the form of irregular waves with a given frequency-angular spectrum [213, 255–259]. Wave spectra used to specify the initial conditions were determined from reanalysis results for respective basins and time intervals. In numerical experiments, waves with large amplitudes were created which, as concluded by the authors, were in relatively good agreement with profiles of measured waves.

6. Conclusions

The question of the nature of anomalously high waves seen in sea wave field records has motivated studies of a much wider range of problems over the last 20 years. Rogue waves have appeared in optics and mathematics, while the problem itself is often treated more broadly as extreme events in the fields of nonlinear waves of a different nature.

Several hundred million instrumentally measured waves are available, including thousands rogue waves; absolute heights of sea waves can reach 30 m. Statistical processing of field measurements has led to contradictory results. Apart from technical questions (a significant number of measured rogue waves have been rejected through formal quality control), the field data processing results can be doubted due to a number of factors: inhomogeneity of data, sampling variability, relatively small size of data arrays, etc. The recording of the instantaneous sea surface, in contrast to classical oceanographic measurements at a single point, offers much richer information, but requires new approaches.

As a result of the studies carried out, the mechanisms of anomalous wave generation have been identified and new physical-mathematical models have been proposed that account for them. A set of basic solutions of integrable equations describing the interaction of soliton structures and the nonlinear stage of modulation wave instability has been constructed and studied. Soliton and breather solutions of the NSE are proposed as standard waveforms for sea-keeping tests [260–262].

The understanding of the role of nonlinear self-modulation processes in stochastic sea wave fields and the importance of accounting for high-order nonlinearity in statistical models have been revisited, and new controlling parameters characterizing the behavior of wave systems have been proposed. In laboratory experiments carried out in hydrodynamical tanks, high-precision equipment has been used which allowed reproducing nonlinear analytical solutions and carrying out wave modeling at large distances. The elaborated fast hydrodynamical models facilitated the accumulation of a large volume of realistic sea wave computations.

Despite the obtained results of a fundamental and applied nature, moving beyond oceanography on a cross-disciplinary level, the problem of sea rogue waves cannot be considered solved. In particular, the significance of the mechanism of wave self-modulation which operates within the framework of physical modeling remains unproven for realistic conditions, and some publications argue that rogue waves can be explained without modulation instability [213]. Twenty years ago, the Norwegians S Haver and O Andersen posed the question whether rogue waves are rare events caused by usual physical mechanisms or are typical manifestations of rarely realizable mechanisms [263]. Based on the data presented in this review, the answer with respect to sea waves is more likely to be the latter. It can explain the disagreement between the conclusions from theoretical modeling, including laboratory experiments, and data from statistical analyses of long-term measurements. The statistical contribution from a rare class of events that correspond to 'anomalous' sea states with a high probability of very high waves might not be very large. Nevertheless, the ability to predict such conditions would be of great practical use.

Several approaches can be proposed for predicting the occurrence of anomalously high waves. With the advent of fast codes for the integration of full and approximate hydrodynamical equations and the increase in the power of computing facilities, real-time forecasting is becoming a reality. The technical realization of simulations of wave evolution for the following few minutes based on radar information on the wave state within a radius of several kilometers seems to be indeed possible [264–266]. Taking into account the relatively narrow horizons of prognostic modeling, crude but fast models can be used, including equations for the envelope and linear equations [267]. The fundamental reliazability of deterministic forecasting follows from the good agreement between the evolution of nonlinear waves in laboratory tanks and the results of computer modeling for times up to $10^1 - 10^2$ wave periods. An estimate of the theoretical limit for deterministic forecasting is about 10^3 wave periods for characteristic sea conditions [268]; forecasting for longer times is only possible in a probabilistic sense.

Another group of approaches is based on numerical indices used to estimate the probability of the occurrence of

extreme waves. For integration with the existing models of operational forecasting, the indicators of hazardous wave states should be computed from spectral data (the BFI and its variants). BFI fields are already being computed at the European Centre for Medium-Range Weather Forecasts (ECMWF); they have been analyzed in Ref. [269]. For nonequilibrium conditions (including the threshold of modulation instability), the link between spectral and statistical characteristics is nonlocal in time, which has not been accounted for so far. Another major difficulty is the short temporal scale of dangerous wave events (the dynamic scale $T_{\rm nl} = \omega_{\rm p}^{-1}\varepsilon^{-2}$, which is tens of minutes or less) and respectively the shorter prediction interval compared to a classical prediction based on kinetic models (several hours or more).

Approaches based on the estimation of wave group properties can be classified as the intermediate, third type of prediction. References [270, 271] proposed and then tested on laboratory data an algorithm to determine the trend of the wave group dynamics through the approximation by the *sech* profile (which coincides with the shape of envelope solitons of the NSE). A more rigorous and accurate, but also more complicated, way of predicting the wave group dynamics is based on the application of the inverse scattering transform under the assumption that the wave dynamics are approximated by an integrable model. Loosely speaking, in this case, a dynamical analog of the BFI is computed at the scales of individual groups. Several variations of this approach have been proposed by different authors for deep water conditions (for the most recent work, see Refs [245, 246, 250, 272, 273]). Soliton analysis of wave fields on shallow water has also been carried out in Ref. [274]. The theoretical description of the probabilistic properties of irregular nonlinear waves based on the data of the spectrum of the associated scattering problem is yet another attractive goal, toward which only the first steps have been made [102, 106].

There are isolated examples of neural networks being used to predict the occurrence of dangerous waves on coasts, but thus far they are not very convincing in our opinion.

The review was written with financial support from the Russian Foundation for Basic Research (RFBR) in the framework of scientific project no. 20-15-50112. The research work of A V S and E N P was supported through a state assignment (topic no. 0030-2021-007) and RFBR grant no. 21-55-15008.

References

1. Draper L *Oceanus* **10** 13 (1964)
2. Mallory J K *Int. Hydrographic Rev.* **51** (2) 99 (1974)
3. Tørum A, Gudmestad O T (Eds) *Water Wave Kinematics* (Dordrecht: Kluwer Acad. Publ., 1990)
4. Lopatukhin L I et al. *Nauchno-Tekh. Sb. Ross. Morskogo Registra Sudokhodstva* (26) 65 (2003)
5. Kharif C, Pelinovsky E, Slunyaev A *Rogue Waves in the Ocean* (Berlin: Springer, 2009)
6. Grigor'ev V G, Gulev S K *Fundament. Priklad. Geofiz.* **4** (4) 18 (2011)
7. Dyachenko A I et al. "Volny-ubiitsy i zadachi ikh issledovaniya" ("Rogue waves and their studies"), in *Mirovoi Okean* (The World Ocean) Vol. 1 *Geologiya i Tektonika Okeana. Katastroficheskie Yavleniya v Okeane* (Geology and Tectorials of the Ocean. Catastrophic Phenomena in the Ocean) (Gen. Ed. L I Lobkovsky) (Moscow: Nauchnyi Mir, 2013)
8. Didenkulova E G *Ocean Coastal Management* **188** 105076 (2020)
9. Nikolkina I, Didenkulova I *Nat. Hazards Earth Syst. Sci.* **11** 2913 (2011)
10. Didenkulova E G, Pelinovsky E N *Dokl. Earth Sci.* **491** 187 (2020); *Dokl. Ross. Akad. Nauk* **491** 97 (2020)
11. Kurkin A A, Pelinovsky E N *Volny-Ubiitsy: Fakty, Teoriya i Modelirovanie* (Rogue Waves, Facts, Theory and Modeling) (Nizhny Novgorog: Nizhegor. Gos. Tekh. Univ., 2004)
12. Dotsenko S F, Ivanov V A *Volny-Ubiitsy* (Rogue Waves) (Sevastopol': MGI NANU, 2006)
13. Shamin R V *Matematicheskie Voprosy Voln-Ubiits* (Mathematical Questions of Rogue Waves) (Synergetics: from the Past to the Future, No 76) (Moscow: LENAND, 2016)
14. Guo B et al. *Rogue Waves: Mathematical Theory and Applications in Physics* (Berlin: Walter de Gruyter GmbH, Hangzhou: Zhejiang Science and Technology Press, 2017) https://doi.org/10.1515/9783110470574
15. Dysthe K, Krogstad H E, Müller P *Annu. Rev. Fluid Mech.* **40** 287 (2008)
16. Slunyaev A, Didenkulova I, Pelinovsky E *Contemp. Phys.* **52** 571 (2011)
17. Onorato M et al. *Phys. Rep.* **528** 47 (2013)
18. Adcock T A A, Taylor P H *Rep. Prog. Phys.* **77** 105901 (2014)
19. Slunyaev A V *Moscow Univ. Phys. Bull.* **72** 236 (2017); *Vestn. Mosk. Univ. Ser. 3 Fiz. Astron.* (3) 33 (2017)
20. Akhmediev N, Pelinovsky E *Eur. Phys. J. Spec. Top.* **185** 1 (2010)
21. Dudley J M et al. *Nat. Photon.* **8** 755 (2014)
22. Dudley J M et al. *Nat. Rev. Phys.* **1** 675 (2019)
23. Holthuijsen L H *Waves in Oceanic and Coastal Waters* (Cambridge: Cambridge Univ. Press, 2007)
24. Haver S, in *Rogue Waves 2004, Proc. of a Workshop, Brest, France, 20–22 October 2004* (Eds M Olagnon, M Prevosto) (Brest: Ifremer, 2005)
25. Massel S R *Ocean Surface Waves: Their Physics and Prediction* (Singapore: World Scientific, 1996)
26. Zakharov V E *J. Appl. Mech. Tech. Phys.* **9** 190 (1968); *Priklad. Mekh. Tekh. Fiz.* (2) 86 (1968)
27. Zakharov V E, Ostrovsky L A *Physica D* **238** 540 (2009)
28. Osborne A R *Nonlinear Ocean Waves and the Inverse Scattering Transform* (New York: Academic Press, 2010)
29. Henderson K L, Peregrine D H, Dold J W *Wave Motion* **29** 341 (1999)
30. Dysthe K B, Trulsen K *Phys. Scr.* (T82) 48 (1999)
31. Kuznetsov E A *Sov. Phys. Dokl.* **22** 507 (1977); *Dokl. Akad. Nauk SSSR* **236** 575 (1977)
32. Peregrine D H *J. Austral. Math. Soc. B* **25** 16 (1983)
33. Akhmediev N N et al. *Sov. Phys. JETP* **62** 894 (1985); *Zh. Eksp. Teor. Fiz.* **89** 1542 (1985)
34. Akhmediev N N, Eleonskii V M, Kulagin N E *Theor. Math. Phys.* **72** 809 (1987); *Teor. Mat. Fiz.* **72** 183 (1987)
35. Akhmediev N, Ankiewicz A, Taki M *Phys. Lett. A* **373** 675 (2009)
36. Cavaleri L et al. (The WISE Group) *Prog. Oceanogr.* **75** 603 (2007)
37. Chalikov D V *Numerical Modeling of Sea Waves* (Cham: Springer, 2016)
38. Chalikov D V *Izv. Atmos. Ocean. Phys.* **56** 312 (2020); *Izv. Ross. Akad. Nauk. Fiz. Atmos. Okeana* **56** 360 (2020)
39. "Cargo ship breaks in half off Turkey", Scuttlebutt Sailing News, Published on February 2, 2021, https://www.sailingscuttlebutt.com/2021/02/02/cargo-ship-breaks-in-half-off-turkey/
40. "Father dies trying to rescue 2 kids swept off beach by wave", U.S. News. The Associated Press, January 5, 2021, https://apnews.com/article/ca-state-wire-1e313a82fc90be476f4061bccd94cbaf
41. Didenkulova I I et al. *Nat. Hazards Earth Syst. Sci.* **6** 1007 (2006)
42. Liu P C *Geofizika* **24** (1) 57 (2007)
43. Liu P C *Nat. Hazards Earth Syst. Sci. Discuss.* **2** 7017 (2014)
44. Baschek B, Imai J *Oceanography* **24** 158 (2011)
45. Candella R N *Nat. Hazards* **83** 211 (2016)
46. O'Brien L et al. *Nat. Hazards Earth Syst. Sci.* **18** 729 (2018)
47. Garcia-Medina G et al. *Nat. Hazards* **94** 583 (2018)
48. Didenkulova I I, Nikolkina I F, Pelinovsky E N *JETP Lett.* **97** 194 (2013); *Pis'ma Zh. Eksp. Teor. Fiz.* **97** 221 (2013)
49. Turton J, Fenna P *Weather* **63** 352 (2008)
50. Barbario F et al. *Prog. Oceanogr.* **175** 139 (2019)
51. Cardone V J et al. *Int. J. Climatol.* **35** 69 (2015)
52. Christou M, Ewans K *J. Phys. Oceanogr.* **44** 2317 (2014)
53. Orzech M D, Wang D *J. Mar. Sci. Eng.* **8** 890 (2020)

54. Cattrell A D et al. *J. Geophys. Res. Oceans* **123** 5624 (2018)
55. Cattrell A D et al. *Sci. Rep.* **9** 4461 (2019)
56. Teutsch I et al. *Nat. Hazards Earth Syst. Sci.* **20** 2665 (2020)
57. Mori N *Ocean Eng.* **31** 165 (2004)
58. Pinho U F, Liu P C, Ribeiro C E P *Geofizika* **21** 53 (2004)
59. Stansell P *Appl. Ocean Res.* **26** 35 (2004)
60. Lavrenov I *Nat. Hazards* **17** 117 (1998)
61. Glejin J et al. *Indian J. Geo-Marine Sci.* **43** 1339 (2014)
62. Didenkulova I *Borel Env. Res.* **16** 138 (2011)
63. Kuznetsov K I et al. *Ekolog. Sist. Prib.* (2) 33 (2014)
64. Divinsky B V et al. *Dokl. Earth Sci.* **395** 438 (2004); *Dokl. Ross. Akad. Nauk* **395** 690 (2004)
65. Karmpadakis I, Swan C *J. Phys. Oceanogr.* **50** 1023 (2020)
66. Benetazzo A et al. *Sci. Rep.* **7** 8276 (2017)
67. Bergamasco F, Benetazzo A *J. Mar. Sci. Eng.* **9** 238 (2021)
68. Cavaleri L et al. *Sci. Data* **8** 37 (2021)
69. Mei C C, Stiassnie M, Yue D K P *Theory and Applications of Ocean Surface Waves* Pt. 1 *Linear Aspects* (Singapore: World Scientific, 2005)
70. Krasitskii V P *J. Fluid Mech.* **272** 1 (1994)
71. Zakharov V *Eur. J. Mech. B* **18** 327 (1999)
72. Zakharov V E *Procedia IUTAM* **26** 43 (2018)
73. Pelinovsky E, Talipova T, Kharif C *Physica D* **147** 83 (2000)
74. White B S, Fornberg B *J. Fluid Mech.* **255** 113 (1998)
75. Johannessen T B, Swan C *Appl. Ocean Res.* **19** 293 (1997)
76. Clauss G *Appl. Ocean Res.* **24** 147 (2002)
77. Ducrozet G, Fink M, Chabchoub A *Phys. Rev. Fluids* **1** 054302 (2016)
78. Tobisch E, Pelinovsky E *J. Phys. A* **53** 345703 (2020)
79. Slunyaev A et al. *Physica D* **173** 77 (2002)
80. Ruban V P *JETP Lett.* **97** 686 (2013); *Pis'ma Zh. Eksp. Teor. Fiz.* **97** 788 (2013)
81. Ruban V P *JETP Lett.* **100** 751 (2014); *Pis'ma Zh. Eksp. Teor. Fiz.* **100** 853 (2014)
82. Stiassnie M, Shemer L *Wave Motion* **41** 307 (2005)
83. Annenkov S Y, Shrira V I *J. Fluid Mech.* **561** 181 (2006)
84. Janssen P A E M *J. Phys. Oceanogr.* **33** 863 (2003)
85. Mori N, Janssen P A E M *J. Phys. Oceanogr.* **36** 1471 (2006)
86. Onorato M et al. *Phys. Rev. Lett.* **86** 5831 (2001)
87. Onorato M et al. *Eur. J. Mech. B* **25** 586 (2006)
88. McLean J W *J. Fluid Mech.* **114** 315 (1982)
89. Alber I E *Proc. R. Soc. Lond. A* **363** 525 (1978)
90. Dyachenko A I, Zakharov V E *JETP Lett.* **81** 255 (2005); *Pis'ma Zh. Eksp. Teor. Fiz.* **81** 318 (2005)
91. Badulin S I, Ivonon D V *Fundament. Priklad. Geofiz.* **5** (1) 37 (2012)
92. Mori N, Onorato M, Janssen P A E M *J. Phys. Oceanogr.* **41** 1484 (2011)
93. Waseda T, Kinoshita T, Tamura H *J. Phys. Oceanogr.* **39** 621 (2009)
94. Xiao W et al. *J. Fluid Mech.* **720** 357 (2013)
95. Ribal et al. *J. Fluid Mech.* **719** 314 (2013)
96. Janssen P *The Interaction of Surface Waves and Wind* (Cambridge: Cambridge Univ. Press, 2004)
97. Pelinovsky E, Sergeeva A *Eur. J. Mech. B* **25** 425 (2006)
98. Mussot A et al. *Opt. Express* **17** 17010 (2009)
99. Slunyaev A V, Pelinovsky E N *Phys. Rev. Lett.* **117** 214501 (2016)
100. Sun Y-H *Phys. Rev. E* **93** 052222 (2016)
101. Ruban V P *JETP Lett.* **102** 650 (2015); *Pis'ma Zh. Eksp. Teor. Fiz.* **102** 739 (2015)
102. Soto-Crespo J M, Devine N, Akhmediev N *Phys. Rev. Lett.* **116** 103901 (2016)
103. Pelinovsky E N, Shurgalina E G, Slunyaev A V, in *Nelineinye Volny 2016* (Eds A M Sergeev, A V Slunyaev) (Nizhny Novgorod: IPF RAN, 2017) p. 279
104. Gelash A A, Agafontsev D S *Phys. Rev. E* **98** 042210 (2018)
105. El G, Tovbis A *Phys. Rev. E* **101** 052207 (2020)
106. Mullyadzhanov R, Gelash A *Phys. Rev. Lett.* **126** 234101 (2021)
107. El G A *J. Stat. Mech.* **2021** 114001 (2021)
108. Agafontsev D S, Zakharov V E *Nonlinearity* **28** 2791 (2015)
109. Agafontsev D S, Zakharov V E *Nonlinearity* **29** 3551 (2016)
110. Kachulin D, Dyachenko A, Zakharov V *Fluids* **5** (2) 67 (2020)
111. Onorato M et al. *Phys. Lett. A* **380** 3173 (2016)
112. Fedele F *J. Fluid Mech.* **782** 25 (2015)
113. Janssen P A E M, Janssen A J E M *J. Fluid Mech.* **859** 790 (2019)
114. Onorato M et al. *Phys. Rev. Lett.* **102** 114502 (2009)
115. Tang T et al. *J. Fluid Mech.* **908** A3 (2021)
116. Annenkov S Y, Shrira V I *Geophys. Res. Lett.* **36** L13603 (2009)
117. Annenkov S Y, Shrira V I *Phys. Rev. Lett.* **102** 024502 (2009)
118. Slunyaev A, Sergeeva A, Pelinovsky E *Physica D* **303** 18 (2015)
119. Janssen T T, Herbers T H C *J. Phys. Oceanogr.* **39** 1948 (2009)
120. Onorato M, Proment D, Toffoli A *Phys. Rev. Lett.* **107** 184502 (2011)
121. Sergeeva A, Pelinovsky E, Talipova T *Nat. Hazards Earth Syst. Sci.* **11** 323 (2011)
122. Ruban V P *JETP Lett.* **95** 486 (2012); *Pis'ma Zh. Eksp. Teor. Fiz.* **95** 550 (2012)
123. Zeng H, Trulsen K *Nat. Hazards Earth Syst. Sci.* **12** 631 (2012)
124. Adcock T A A, Taylor P H *Int. J. Offshore Polar Eng.* **21** 8 (2011)
125. Ducrozet G, Slunyaev A V, Stepanyants Y A *Phys. Fluids* **33** 066606 (2021)
126. Trulsen K et al. *J. Fluid Mech.* **882** R2 (2020)
127. Zheng Y K et al. *Phys. Rev. Fluids* **5** 064804 (2020)
128. Zhang J, Benoit M *J. Fluid Mech.* **912** A28 (2021)
129. Li Y et al. *J. Fluid Mech.* **915** A71 (2021)
130. Peregrine D H *Adv. Appl. Math.* **16** 9 (1976)
131. Basovich A Ya, Talanov V I *Izv. Akad. Nauk SSSR. Fiz. Atmos. Okeana* **13** 766 (1977)
132. Moreira R M, Peregrine D H *J. Fluid Mech.* **691** 1 (2012)
133. Shrira V I, Slunyaev A V *J. Fluid Mech.* **738** 65 (2014)
134. Pelinovsky E, Polukhina O, Kurkin A *Eur. Phys. J. Spec. Top.* **185** 35 (2010)
135. Shrira V I, Slunyaev A V *Phys. Rev. E* **89** 041002 (2014)
136. Deconinck B, Segal B L *Physica D* **346** 1 (2017)
137. Chen J, Pelinovsky D E, White R E *Physica D* **405** 132378 (2020)
138. Zakharov V E, Shabat A B *Sov. Phys. JETP* **34** 62 (1972); *Zh. Eksp. Teor. Fiz.* **61** 118 (1971)
139. Ablowitz M J et al. *Stud. Appl. Math.* **53** 249 (1974)
140. Biondini G, Mantzavinos D *Commun. Pure Appl. Math.* **70** 2300 (2017)
141. Grinevich P G, Santini P M *Nonlinearity* **31** 5258 (2018)
142. Kedziora D J, Ankiewicz A, Akhmediev N *Phys. Rev. E* **88** 013207 (2013)
143. Matveev V B, Smirnov A O *J. Math. Phys.* **59** 091419 (2018)
144. Chen J, Pelinovsky D E, White R *Phys. Rev. E* **100** 052219 (2019)
145. Tajiri M, Watanabe Y *Phys. Rev. E* **57** 3510 (1998)
146. Slunyaev A *Eur. J. Mech. B* **25** 621 (2006)
147. Zakharov V E, Gelash A A *Phys. Rev. Lett.* **111** 054101 (2013)
148. Garnier J, Kalimeris K *J. Phys. A* **45** 035202 (2012)
149. Biondini G, Kovacic G *J. Math. Phys.* **55** 031506 (2014)
150. Bilman D, Miller P D *Commun. Pure Appl. Math.* **72** 1722 (2019)
151. Klaus M, Pelinovsky D E, Rothos V M *J. Nonlin. Sci.* **16** 1 (2006)
152. Klein C, Haragus M *Ann. Math. Sci. Appl.* **2** 217 (2017)
153. Calini A, Schober C M, Strawn M *Appl. Numer. Math.* **141** 36 (2019)
154. Cuevas-Maraver J et al. *Phys. Rev. E* **96** 012202 (2017)
155. Calini A, Schober C M *Nonlinearity* **25** R99 (2012)
156. Grinevich P G, Santini P M *Nonlinearity* **34** 8331 (2021); Haragus M, Pelinovsky D E *J. Nonlinear. Sci.* **32** 66 (2022)
157. Alejo M A, Fanelli L, Munoz C *Front. Phys.* **8** 591995 (2020)
158. Pelinovsky D E *Front. Phys.* **9** 599146 (2021)
159. Kedziora D J, Ankiewicz A, Akhmediev N *Eur. Phys. J. Spec. Top.* **223** 43 (2014)
160. Chen J, Pelinovsky D E *Proc. R. Soc. Lond. A* **474** 20170814 (2018)
161. Feng B F, Ling L, Takahashi D A *Stud. Appl. Math.* **144** 46 (2020)
162. Xu G et al. *Phys. Rev. Res.* **2** 033528 (2020)
163. Baronio F et al. *Phys. Rev. Lett.* **113** 034101 (2014)
164. Baronio F *Phys. Rev. A* **91** 033804 (2015)
165. Mancic A et al. *Phys. Rev. E* **98** 012209 (2018)
166. Pelinovsky D E, White R E *Proc. R. Soc. Lond. A* **476** 20200490 (2020)
167. Marangell R, Miller P D *Physica D* **308** 87 (2015)
168. Deconinck B, McGill P, Segal B L *Physica D* **360** 17 (2017)
169. Chen J, Pelinovsky D E *Nonlinearity* **31** 1955 (2018)
170. Bertola M, El G A, Tovbis A *Proc. R. Soc. Lod. A* **472** 20160340 (2016)
171. Wright O C *Physica D* **321** 16 (2016)
172. Bertola M, Tovbis A *Commun. Math. Phys.* **354** 525 (2017)
173. Wright O C *Nonlinearity* **32** 1929 (2019)

174. Soto-Crespo J M, Denive N, Akhmediev N *Phys. Rev. A* **96** 023825 (2017)
175. Kimmoun O et al. *Sci. Rep.* **6** 28516 (2016)
176. Vanderhaegen G et al. *Opt. Lett.* **45** 3757 (2020)
177. Conforti M et al. *Phys. Rev. A* **101** 023843 (2020)
178. Gramstad O, Stiassnie M *J. Fluid Mech.* **718** 280 (2013)
179. Annenkov S Y, Shrira V I *J. Fluid Mech.* **844** 766 (2018)
180. Slunyaev A V *J. Exp. Theor. Phys.* **101** 926 (2005); *Zh. Eksp. Teor. Fiz.* **128** 1061 (2005)
181. Sedletsky Yu V *Ukr. J. Phys.* **66** 41 (2021)
182. Trulsen K et al. *Phys. Fluids* **12** 2432 (2000)
183. Gramstad O, Trulsen K *J. Fluid Mech.* **670** 404 (2011)
184. Slunyaev A, Pelinovsky E, Guedes Soares C *J. OMAE* **136** 011302 (2014)
185. Dyachenko A I *Dokl. Math.* **63** 115 (2001); *Dokl. Ross. Akad. Nauk* **376** 27 (2001)
186. Zakharov V E, Dyachenko A I, Vasilyev O A *Eur. J. Mech. B* **21** 283 (2002)
187. Chalikov D *Nonlin. Proc. Geophys.* **12** 671 (2005)
188. Ruban V P *Phys. Rev. E* **71** 055303 (2005)
189. Ruban V P *Phys. Rev. E* **81** 056303 (2010)
190. Lushnikov P M, Dyachenko S A, Silantyev D A *Proc. R. Soc. Lond. A* **473** 20170198 (2017)
191. Dyachenko et al. *Proc. R. Soc. Lond. A* **476** 20200811 (2021)
192. Dommermuth D, Yue D K P *J. Fluid Mech.* **184** 267 (1987)
193. West et al. *J. Geophys. Res.* **92** 11803 (1987)
194. Onorato M, Osborne A R, Serio M *Eur. J. Mech. B* **26** 43 (2007)
195. Ducrozet G et al. *Comput. Phys. Commun.* **203** 245 (2016)
196. Gouin M, Ducrozet G, Ferrant P *Eur. J. Mech. B* **57** 115 (2016)
197. Chalikov D V, Babanin A V, Sanina E *Ocean Dyn.* **64** 1469 (2014)
198. Dyachenko A I, Zakharov V E *JETP Lett.* **93** 701 (2011); *Pis'ma Zh. Eksp. Teor. Fiz.* **93** 782 (2011)
199. Dyachenko A I, Kachulin D I, Zakharov V E *J. Fluid Mech.* **828** 661 (2017)
200. Dyachenko A I *Stud. Appl. Math.* **144** 493 (2020)
201. Babanin A *Breaking and Dissipation of Ocean Surface Waves* (Cambridge: Cambridge Univ. Press, 2011)
202. Slunyaev A, Kokorina A *Water Waves* **2** 243 (2020)
203. Zakharov V E, Shamin R V *JETP Lett.* **96** 66 (2012); *Pis'ma Zh. Eksp. Teor. Fiz.* **96** 68 (2012)
204. Shamin R V, Yudin A V *Math. Models Comput. Simul.* **9** (2) 176 (2017); *Matem. Model.* **28** (9) 31 (2016)
205. Zakharov V E, Shamin R V *JETP Lett.* **91** 62 (2010); *Pis'ma Zh. Eksp. Teor. Fiz.* **91** 68 (2010)
206. Kirezci C, Babanin A V, Chalikov D V *Ocean Eng.* **231** 108715 (2021)
207. Shemer L, Sergeeva A, Slunyaev A *Phys. Fluids* **22** 016601 (2010)
208. Shemer L, Sergeeva A, Liberzon D *J. Geophys. Res.* **115** 12039 (2010)
209. Slunyaev A V, Sergeeva A V *JETP Lett.* **94** 779 (2011); *Pis'ma Zh. Eksp. Teor. Fiz.* **94** 779 (2011)
210. Slunyaev A V *Phys. Rev. E* **101** 062214 (2020)
211. Annenkov S Y, Shrira V I *J. Phys. Oceanogr.* **44** 1582 (2014)
212. Andrade D, Stiassnie M *Wave Motion* **97** 102581 (2020)
213. Fedele F et al. *Sci. Rep.* **6** 27715 (2016)
214. Chalikov D, Bulgakov K *J. Ocean Eng. Mar. Energy* **3** 417 (2017)
215. Arena F *Ocean Eng.* **32** 1311 (2005)
216. Petrova P, Arena F, Guedes Soares C *Ocean Eng.* **38** 1640 (2011)
217. Ruban V P *Phys. Rev. Lett.* **99** 044502 (2007)
218. Chalikov D V *Fundament. Priklad. Geofiz.* **5** (1) 5 (2012)
219. Sergeeva A, Slunyaev A *Nat. Hazards Earth Syst. Sci.* **13** 1759 (2013)
220. Zakharov V E, Shamin R V, Yudin A V *JETP Lett.* **99** 514 (2014); *Pis'ma Zh. Eksp. Teor. Fiz.* **99** 59 (2014)
221. Zakharov V E, Shamin R V, Yudin A V *Dokl. Earth Sci.* **462** 484 (2015); *Dokl. Ross. Akad. Nauk* **462** 100 (2015)
222. Adcock T A A, Taylor P H, Draper S *Proc. R. Soc. Lond. A* **471** 20150660 (2015)
223. Adcock T A A, Taylor P H, Draper S *Phys. Fluids* **28** 106601 (2016)
224. Slunyaev A, Sergeeva A, Didenkulova I *Nat. Hazards* **84** 549 (2016)
225. Slunyaev A V, Kokorina A V *Izv. Atmos. Ocean. Phys.* **56** 179 (2020); *Izv. Ross. Akad. Nauk. Fiz. Atm. Okeana* **56** 210 (2020)
226. Ruban V P *JETP Lett.* **94** 177 (2011); *Pis'ma Zh. Eksp. Teor. Fiz.* **94** 194 (2011)
227. Kokorina A, Slunyaev A *Fluids* **4** 70 (2019)
228. Fujimoto W, Waseda T, Webb A *Ocean Dyn.* **69** 101 (2019)
229. Dyachenko A I, Zakharov V E *JETP Lett.* **88** 307 (2008); *Pis'ma Zh. Eksp. Teor. Fiz.* **88** 356 (2008)
230. Slunyaev A V *JETP* **109** 676 (2009); *Zh. Eksp. Teor. Fiz.* **136** 785 (2009)
231. Slunyaev A et al. *Phys. Fluids* **25** 067105 (2013)
232. Slunyaev A, Klein M, Clauss G F *Phys. Fluids* **29** 047103 (2017)
233. Dyachenko A I, Kachulin D I, Zakharov V E *Nat. Hazards Earth Syst. Sci.* **13** 3205 (2013)
234. Kachulin D, Dyachenko A, Gelash A *Fluids* **4** 83 (2019)
235. Kachulin D, Dyachenko A, Dremov S *Fluids* **5** 65 (2020)
236. Chabchoub A, Hoffmann N P, Akhmediev N *Phys. Rev. Lett.* **106** 204502 (2011)
237. Chabchoub A et al. *Phys. Rev. X* **2** 011015 (2012)
238. Chabchoub A et al. *Phys. Fluids* **25** 101704 (2013)
239. Slunyaev A et al. *Phys. Rev. E* **88** 012909 (2013)
240. Slunyaev A V, Shrira V I *J. Fluid Mech.* **735** 203 (2013)
241. Shemer L, Alperovich L *Phys. Fluids* **25** 051701 (2013)
242. Viotti C et al. *Phys. Rev. E* **87** 063001 (2013)
243. Slunyaev A V, Kokorina A V *J. Ocean Eng. Mar. Energy* **3** 395 (2017)
244. Cazaubiel A et al. *Phys. Rev. Fluids* **3** 114802 (2018)
245. Osborne A et al. *Ocean Dyn.* **69** 187 (2019)
246. Suret P et al. *Phys. Rev. Lett.* **125** 264101 (2020)
247. Tikan A *Phys. Rev. E* **101** 012209 (2020)
248. Wang A et al. *Phys. Fluids* **32** 087109 (2020)
249. Agafontsev D S, Gelash A A *Front. Phys.* **9** 610896 (2021)
250. Slunyaev A V *Phys. Fluids* **33** 036606 (2021)
251. Sergeeva A et al. *Nat. Hazards Earth Syst. Sci.* **14** 861 (2014)
252. Adcock T A A et al. *Proc. R. Soc. Lond. A* **467** 3004 (2011)
253. Clauss G F, Klein M *J. Offshore Mech. Arct. Eng.* **131** 041001 (2009)
254. McAllister M L et al. *J. Fluid Mech.* **860** 767 (2019)
255. Bitner-Gregersen E M et al. *Nat. Hazards Earth Syst. Sci.* **14** 1407 (2014)
256. Fedele F, Lugni C, Chawla A *Sci. Rep.* **7** 11188 (2017)
257. Donelan M A, Magnusson A K *Sci. Rep.* **7** 44124 (2017)
258. Kokina T, Dias F *J. Mar. Sci. Eng.* **8** 1023 (2020)
259. Innocenti A, Onorato M, Brandini C *J. Mar. Sci. Eng.* **9** 422 (2021)
260. Onorato M et al. *PLOS One* **8** e54629 (2013)
261. Klein M et al. *Ocean Eng.* **128** 199 (2016)
262. Klein M, Clauss G F, Hoffmann N *Ocean Eng.* **234** 109271 (2021)
263. Haver S, Andersen O J, in *Proc. of the Tenth (2000) Intern. Offshore and Polar Engineering Conf. ISOPE-2000, Seattle, USA, May 27 – June 2 2000* (Cupertino, CA: The Intern. Soc. of Offshore and Polar Engineers, 2000) p. 123
264. van Groesen E, Turnip P, Kurnia R *J. Ocean Eng. Mar. Energy* **3** 233 (2017)
265. Köllisch N et al. *Ocean Eng.* **157** 387 (2018)
266. Klein M et al. *Fluids* **5** (1) 9 (2020)
267. Ruban V P *JETP Lett.* **103** 568 (2016); *Pis'ma Zh. Eksp. Teor. Fiz.* **103** 647 (2016)
268. Annenkov S Yu, Shrira V I *J. Fluid Mech.* **449** 341 (2001)
269. Ponce de León S, Guedes Soares C *Ocean Modelling* **81** 78 (2014)
270. Cousins W, Sapsis T P *J. Fluid Mech.* **790** 368 (2016)
271. Cousins W et al. *Phys. Rev. E* **99** 032201 (2019)
272. Randoux S, Suret P, El G *Sci. Rep.* **6** 29238 (2016)
273. Calini A, Schober C M *Wave Motion* **71** 5 (2017)
274. Brühl M, Oumeraci H *Appl. Ocean Res.* **61** 81 (2016)